LASER POWDER BED FUSION PROCESSING OF ALUMINUM POWDERS
CONTAINING IRON AND NICKEL

by

Jonathan Hierlihy

Submitted in partial fulfilment of the requirements
for the degree of Masters of Applied Science

at

Dalhousie University
Halifax, Nova Scotia
August 2020

TABLE OF CONTENTS

LIST OF TABLES

LIST OF FIGURES

ABSTRACT

Laser powder bed fusion additive manufacturing (PBF-AM) uses laser energy to selectively melt powder particles within a powder bed in a successive layer-wise fashion. Fabricating parts in this manner fosters significant design freedom such that many of the geometrical constraints imposed in traditional metal forming technologies no longer apply. The highly non-equilibrium nature of the process also offers distinct opportunities to develop novel materials with unique microstructures and properties [1]. Industrially, this has now been leveraged successfully for Ti-, Ni-, Fe-, Al- and CoCr-based alloys. However, in all instances, the number of alloys exploited in commercial PBF-AM operations remains limited. Al-based alloys are a prime example in that over 600 formulations are compatible with traditional metal forming technologies, while as of 2018, only a singular alloy (AlSi10Mg) was recognized by ASTM for use in PBF-AM [2]. This alloy is responsive to PBF-AM as densities upwards of 99.8% theoretical have been achieved with minimal defects [3]. Work on other alloys has typically been challenging as most suffer from solidification cracking [4].

Al-based systems containing transition metal (TM) additions are becoming a growing focus in PBF-AM alloy development, as many TM additions form coherent, strengthening trialuminide intermetallics (Al_3M) [5], [6]. Additionally, the low solid solubility and diffusivity of TMs in aluminum inhibits dissolution and coarsening of their aluminides at elevated temperatures [7]. Additions of Fe and Ni, are known to produce such intermetallics [7]. In fact, a number thermally stable Al-based powder metallurgy alloys are based on the Al-Fe and Al-Ni systems [8]. However, the non-equilibrium nature of PBF-AM complicates the alloy development process significantly. In particular, the high solidification front velocities (SFVs) and cooling rates typical of PBF-AM are known to extend the solid solubility of alloying additions and form metastable phases [9]–[12]. This greatly reduces the direct applicability of equilibrium-based resources such as phase diagrams and thermodynamic modeling software. Despite this, the effects of alloying additions on solidification cracking during PBF-AM can be compared quantitatively using partitioning coefficients and relative potency factors (RPFs) [8], [13], [14], however they must also include considerations for the high SFVs present.

In this context, the objective of this study was to evaluate the viability of Fe and Ni additions as well as to characterize and compare the amenability of the Al-Fe and Al-Ni systems to the PBF-AM process. In doing so, gas atomized Al-1Fe and Al-1Ni (wt.%) powders were processed by PBF-AM with varying laser powers, scan speeds, and hatch spacing and the resulting microstructures (OM, SEM, EDS, XRD) and physical properties (hardness, density, surface roughness) were characterized. It was shown that Al-1Fe was more responsive to processing as it densified to 99.0% theoretical and had a hardness of 95 HRH. Conversely, Al-1Ni only reached 97.8% theoretical density and a peak hardness of 78 HRH. The diminished properties of the Al-1Ni powder were attributed to solidification cracking behaviour not observed in the Al-1Fe specimens. SFV-dependent partitioning coefficients and RPFs were then estimated and showed that Al-1Fe was less likely to exhibit undesirable solidification conditions known to cause solidification cracking.

LIST OF ABBREVIATIONS AND SYMBOLS USED

AEC	Applied energy correlation
Al_3M	Trialuminide intermetallic
AM	Additive manufacturing
a_o	Interatomic distance of the primary solidification phase
at.%	Atomic percent
b	Magnitude of a Burger's vector
C_e^{α}	Equilibrium solubility of a solute species in the matrix phase
C_e^{β}	Equilibrium solubility of a solute species in a precipitate phase
C_L	Solute content of the liquid phase at the solid-liquid interface
C_s	Solute content of the solid phase at the solid-liquid interface
CTE	Coefficient of thermal expansion
CW	Continuous wave
d	Laser spot size
D	Solid diffusivity of a solute species in the matrix phase
D_L	Liquid diffusivity
DSC	Differential scanning calorimetry
E_A	Andrew's Number
EDS	Electron dispersive x-ray spectroscopy
E_L	Linear energy density
E_S	Surface energy density
E_V	Volumetric energy density
G	Thermal gradient
h	Hatch spacing
ICDD	International Center for Diffraction Data
ICP-OES	Inductively coupled plasma – optical emission spectroscopy
k	Partitioning coefficient
k_{eq}	Equilibrium partitioning coefficient
k_o	Rate constant for precipitate coarsening by Ostwald ripening
k_v	Solidification front velocity-dependent partitioning coefficient
M	Taylor Factor of the matrix phase
m_L	Liquidus slope
m_L^v	Solidification front velocity-dependent liquidus slope
OM	Optical microscopy
P	Laser power
PBF-AM	Laser powder bed fusion additive manufacturing
PSD	Particle size distribution
R	Growth Rate
$\bar{R}$	Mean planar radius of a precipitate
REM	Rare earth metal

RPF	Relative potency factor
RSP	Rapid solidification process/processing
R_t	Precipitate radius at time t
S_a	Surface area roughness
SEM	Scanning electron microscopy
SFV	Solidification front velocity
T	Temperature
t	Time
T_L	Liquidus temperature
TM	Transition metal
T_q	Actual liquid temperature at the solid-liquid interface
T_S	Solidus temperature
UTS	Ultimate tensile strength
v	Laser scan speed
v_D	Diffusive speed of solute across the solid-liquid interface
w	Beam width at waist
wt.%	Weight percent
XRD	X-ray diffraction
YS	Yield strength
λ	Wavelength
λ_d	Effective distance between precipitates
ν	Poisson's ratio
σ	Interfacial energy between a precipitate and the matrix phase
σ_{Or}	Stress required to form an Orowan dislocation loop

ACKNOWLEDGEMENTS

1 INTRODUCTION

Additive manufacturing (AM) is said to be a revolutionary technology that will disrupt the manufacturing industry. The basic principle of AM is to directly produce a part from a three-dimensional digital model, without the need for extensive process planning [15]. AM manufactures parts in a layer-by-layer fashion, as opposed to subtractive manufacturing processes, which involve removing material from a bulk [16]. This gives designers and engineers the freedom to fabricate and test multiple prototype iterations simultaneously [1].

The use of AM can eliminate the need for multiple machining and/or forming processes and reduces material waste, making AM both a cost-saving and environmentally friendly process compared to traditional manufacturing methods [1]. AM has been used in a wide range of applications in the transport, military, electronics and medical fields, and was a 2.2 billion USD industry as of 2016 [1], [17].

AM processes can be subdivided into 7 subclasses, including binder jetting, direct energy deposition, material extrusion, material jetting, powder bed fusion (PBF-AM), sheet lamination, and vat polymerization [16]. Of these 7 classes, 3 use lasers to facilitate the layer-wise production of a part: PBF-AM, direct energy deposition and vat polymerization [16], [17].

1.1 Laser Powder Bed Fusion Additive Manufacturing

PBF-AM processes use a laser to fuse powder at selected locations within a powder bed and at controlled speeds in a layer-wise fashion. Lasers are used as the primary energy source for fusion as they produce a highly monochromatic beam of high-energy radiation that can propagate over long distances without critical divergence. This allows the beam to effectively transfer energy to the powder substrate while remaining focused into a small spot [18]. This is critical as spherical powders in the 20 to 63 μm size range [19] are

typically used in PBF-AM processes to improve final part density, print resolution, and surface finish [15].

The preferred laser types for PBF-AM technology are Nd:YAG solid state and Yb-doped fiber lasers [18]. They can achieve powers from 1 W to 6 kW [18] and operate wavelengths of 1064 nm and 1030 to 1070 nm [18], respectively.

1.1.1   The Laser Powder Bed Fusion Process

The PBF-AM process (Figure 1) begins by forming a powder bed above the build platform. To do this, the build platform is first lowered one layer thickness. A feed cartridge containing powder is raised to make powder available to a powder recoater that applies a smooth, thin layer onto the powder bed and pushes excess powder into an overflow container. Powder recoaters are commonly either a counter-rotating powder leveling roller like that shown in Figure 1 or some form of a rigid blade. Layers may also be deposited by a top-fed hopper that makes powder available to an incorporated recoater as it passes over the bed [15].

If necessary, the powder is then be heated with a heater from above (IR heater in Figure 1) or by resistive heating elements below the build platform. Desired areas within the powder bed are then selectively scanned by a laser to fuse particles within the new layer to one another as well as previous layers below. This process is repeated for each layer until the final part is produced. Finished parts are then allowed to cool, depowered and removed from the printer, separated from the build plate, and finished with subsequent processing (i.e. annealing, machining, etc.) as required [15].
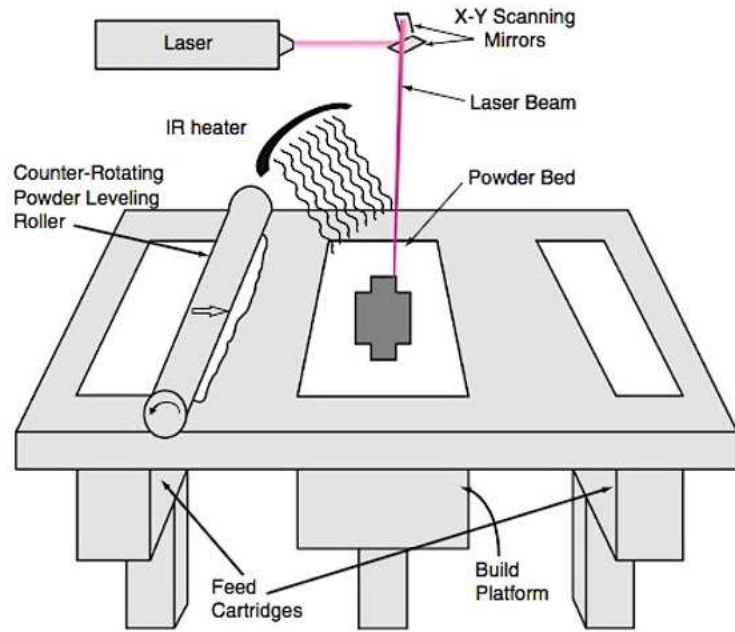
Figure 1. A basic schematic showing the parts of a laser powder bed fusion printer [15].

1.1.2   *Process Parameters and Their Influence*

Process parameters in PBF-AM can be subdivided into 4 categories: Laser-related, scan-related, powder-related, and temperature-related parameters (Figure 2) [15], [20]. In the most basic sense, 14 parameters fall within these 4 categories. Many of these are interrelated, meaning changes to one may require the adjustment of others to attain a similar final product [15]. Therefore, many process variables are often combined into Applied Energy Correlations (AECs) which will be discussed once all relevant parameters have been introduced [15], [18], [21].
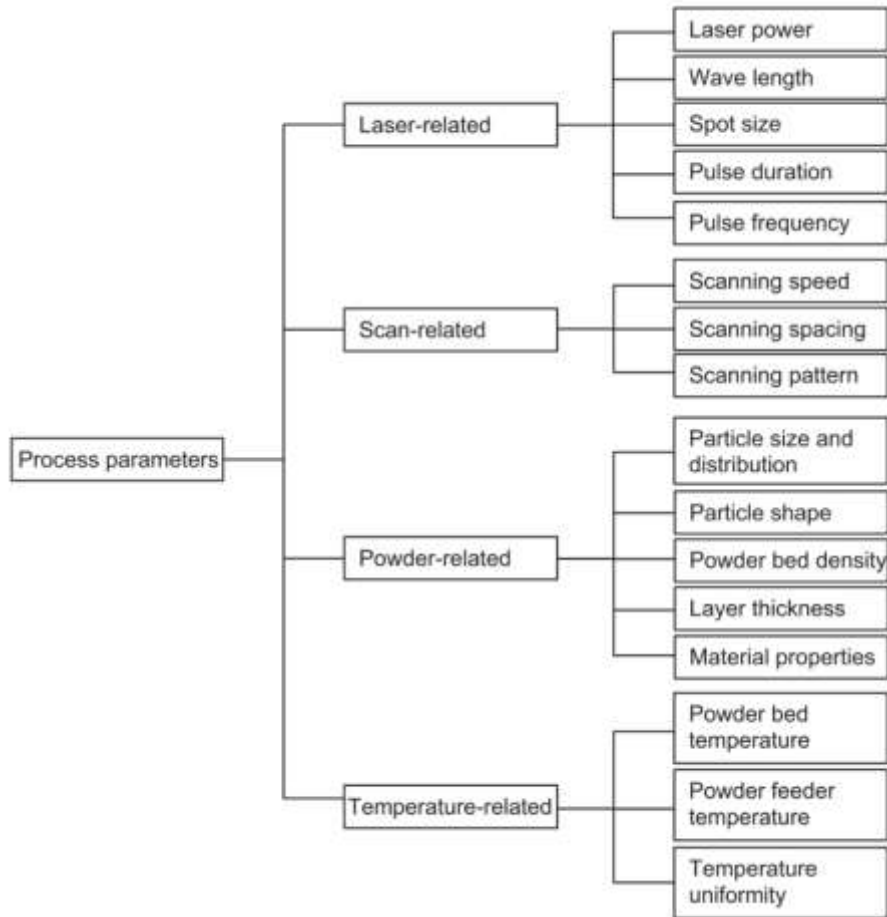
Figure 2. Overview of the parameters encountered in PBF-AM [20].

1.1.2.1 Laser-Related Parameters

When considering laser-related parameters, it is important to remember that only a fraction of the incident beam energy is absorbed while the rest is reflected. The energy absorbed is dependent not only on the traits of the laser itself, but also on certain parameters from each of the other categories such as absorptivity of the material, scan speed, layer thickness, hatch spacing, and temperature [18].

The most important laser-related parameters are the wavelength of the beam and the laser power. Laser power is defined as the amount of photon energy being delivered per unit time and dictates the amount incident energy provided to facilitate fusion [22] which is

partially dictated by the wavelength of the beam [18]. Metals most readily absorb smaller wavelengths, meaning the use of a Nd:YAG or Yb-fiber laser (~1070 nm) is preferable to a CO_2 laser (~10.6 um) [18]. Conversely, if a longer wavelength was used, the requisite laser power would need to be larger to allow the same amount of effective energy to be transferred the powder, possibly making the process less efficient [18].

In PBF-AM processes, the beam is focused over a small circular area. The diameter of this area is defined as spot size and is a controllable parameter [18]. Attainable spot size generally depends on the optics used [18]. The minimum theoretical spot size is the wavelength [18] and dictates the lowest resolution of a PBF-AM process that is theoretically attainable. However, it is worth noting that this differs from the practical minimum printer resolution, which is almost always limited by other factors [18].

Many PBF-AM systems also allow the laser to be operated in continuous wave (CW) or in a modulated mode. In the former, the laser remains on continually as it is scanned over the surface of the powder bed. Conversely, when a laser is modulated, it is toggled on/off to output the desired power but only for a short time, known as a pulse duration. Such pulses are then repeated at a fixed time interval known as the pulse frequency [18]. As pulse duration and frequency are increased, energy delivered to the material per unit time is increased, eventually becoming comparable to that achieved in the CW mode of operation [18]. In other scenarios, a true pulsed laser can be employed. These lasers generally deliver a much higher peak energy output than that achievable with a CW/modulated laser, which can offer advantages [18], [22], [23]. For instance, when the powder is hit with a very high energy, short duration pulse, it heats up instantaneously, and tends to dissipate less heat into the surrounding material, as is observed in CW lasers [18]. However, as pulsed lasers have significant limitations when it comes to the attainable build speed, CW/modulated units currently dominate the PBF-AM market.

1.1.2.2   Scan-Related Parameters

Scan speed is defined as the speed at which the laser is tracked across the powder bed [1], [15]. Scan speeds are typically between 0.1 to 5 ms^{-1} [1] and the value employed can influence the presence of defects. This is because it is critical in determining the amount of energy delivered to the powder, and consequently the thermal conditions and morphology of the melt pool generated [20].

Scan spacing, also referred to as hatch spacing, is the distance between the centerlines of adjacent laser passes (Figure 3) [1], [15]. Hatch spacings are typically chosen so that the melt pools of adjacent tracks overlap as well as to foster desirable melt pool dynamics as well as improved inter-layer fusion and solidification behaviour [15]. Multiple passes of each layer may also be done at a higher scan speed or reduced power to mitigate common defects [15].

Scan patterns typically feature contours and filling (Figure 3) [15]. Contours form the outline of the part cross-section for a given layer. They are typically processed under conditions that equate to optimized surface properties [15]. Filling follows contouring and is often done using a meandering raster where the laser sweeps back and forth across the part while each laser path is offset in a perpendicular direction by one hatch spacing [15]. Another common rastering technique used is a chessboard approach, where each layer is subdivided into squares and rastered in random directions [15]. This helps mitigate the formation of residual stresses in preferential directions and is mostly used for metals [15].
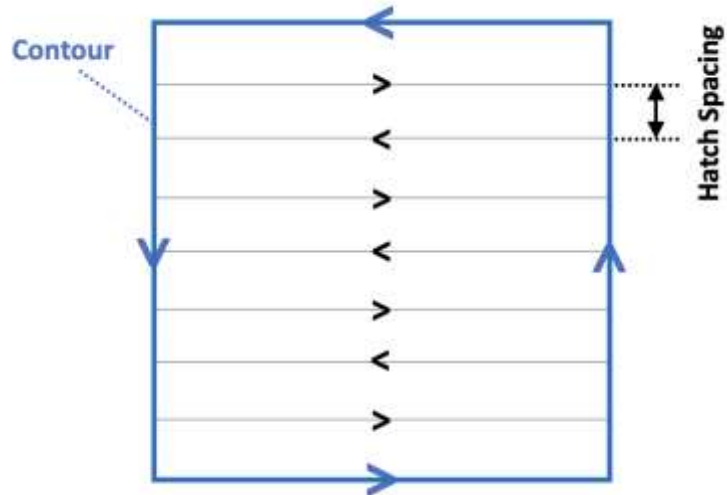
Figure 3. Contours and hatch spacing involved in a basic meandering scan strategy.

1.1.2.3 Powder-Related Parameters

Powder bed density is an important factor to consider when trying to obtain a dense final part with well-bonded layers and minimal defects [15], [19]. It is determined by particle morphology, size, and particle size distribution (PSD), as well as the spreading mechanism used [15], [19]. The powder traits play a significant role in powder performance and processability, which generally determines flowability and packing efficiency, making them the most important properties relative to forming a dense powder bed [19]. Powder bed density affects the fusion of subsequent layers and the density of the final part, which in turn drive the ultimate mechanical properties, concentration of porosity, residual stress state, and surface finish of a printed part [19].

Particle size is one of the most studied powder-related variables [19]. The general consensus is that smaller particle sizes are preferable to large ones, as they require less energy input to invoke fusion [1]. They also manifest increases in powder bed and finished part densities as well as practical print resolutions which leads to improvements in surface roughness [19]. They are not, however, without issue. Smaller particle sizes are more prone to agglomerations due to amplified effects of electrostatic forces and interparticle friction

7

on their smaller mass [19]. Such agglomerates can hinder flowability and the ability to spread a dense, uniform powder layer; the net effect observed as diminished properties [19]. The formation of agglomerates may also cause defects in the finished part, as they behave like large, non-spherical particles during scanning [19]. Small particles also have a larger surface area which has been seen to increase reflectivity, hindering absorption of laser energy by the powder [19]. While overcoming this by increasing laser power may seem viable, exposing small particles to higher energy may also intensify the evaporation of volatile components, increase the amount of spatter, and/or promote the formation of a condensate cloud that can attenuate the incident laser beam and alter the chemistry of the final product [19].

Morphology is another powder trait that is commonly studied. Generally speaking, particles that maintain a spherical shape are typically the most desirable for use in PBF-AM. Critically, this shape equates to a minimized number of inter-particle contacts coupled with a relatively low surface roughness; the combined effect of which reduces interparticle friction. Accordingly, spherical powders typically exhibit excellent flow, manifest increased powder bed densities, and as such, superior final part density [19].

PSD is typically chosen to maximize packing density, which is done including smaller particles that fill the spaces between larger ones [19]. In PBF-AM, a broader PSD generally leads to increased part density and decreased surface roughness, where a narrow PSD generally leads to improved mechanical properties [19]. The upper threshold of the PSD is typically determined by the layer thickness being used [19]. In this sense, if the particle size exceeds layer thickness, they will exert a shear force on the bed that prevents the attenuation of the smooth, thin layer sought [19].

Layer thickness is the depth of powder deposited onto the powder bed during each pass. It has a large influence on the densities of the bed itself and the final product, as well as the surface roughness of the finished part [19]. As layer thickness is increased, the bed density is decreased, due to non-optimal packing, which in turn leads to decreased part density

[19]. Increasing layer thickness also leads to a rougher surface finish due to an increased amount of larger particles in the bed [19].

1.1.2.4 Temperature-Related Parameters

Key parameters in this category are the pre-heating temperatures of the powder bed and powder feeder and the respective uniformity therein. Preheating is frequently advantageous as it acts to lower the required laser power and lessen thermal gradients that minimize residual stresses and warping [1], [15]. The build platform and feeders may be heated by integrated resistive heaters, while the bed may also be heated by external heaters [15]. Temperature uniformity is also an important aspect of PBF processes, as it helps ensure repeatable results [15].

Melt pool temperature and thermal gradient are also known to impact the as-printed microstructure [20]. The former is dependent on laser power, such that it increases significantly with rising laser power and slightly with decreasing scan speed [20]. The thermal gradient also increases with increasing laser power, the effect is more pronounced in materials with low thermal conductivity [20].

Melt pool geometry and lifetime are also often considered [20]. The geometry encompasses the length, width and depth of the liquid melt pool. Melt pool depth is known to increase as more energy per unit is applied volume [20], while width is shown to decrease and length to increase with increasing scan speed [20]. The melt lifetime is used to describe the amount of time the melt pool is in existence at temperatures above the solidus temperature, and is found to increase with upward adjustments in laser power and decreased scan speeds [20].

1.1.2.5 Material Properties Relevant to PBF-AM

An understanding of material properties relevant to the PBF-AM processes is paramount to attaining viable end products. Intrinsic material properties such as absorptivity, thermal

conductivity and surface chemistry, as well as melt characteristic including viscosity, surface tension, and wettability, are all extremely important and require careful consideration [1], [19]. For instance, thermally conductive materials may conduct heat to surrounding solids before fusion is achieved and therefore often require greater energy inputs [1], [19].

Absorptivity is defined as the ratio of absorbed radiation to incident radiation, and can be critical in determining the optimal process window for a given material [1]. Accordingly, it is one of the most important material properties to consider in PBF-AM processes as powder particles must readily absorb the incident energy if they are to be melted. However, the efficiency of this process can vary widely for different metals and alloys upon exposure to radiation of a prescribed wavelength [1] and must be accounted for appropriately.

As previously stated, absorptivity is inversely proportional to wavelength for metals. Interestingly, the opposite is true for oxides [1]. Hence, the presence of surface oxides on powder particles can lessen absorptivity. Surface oxides (and other undesirable powder surface attributes such as moisture and dissolved gasses) also contribute to the aforementioned agglomeration behaviour and can degrade melt pool quality [1], [15], [19].

The melt properties of the material often influence the fusion of particles and the presence of defects [1], [19]. The quality of a melt depends heavily on the viscosity and wettability of the melt pool. Viscosity is dictated by temperature and alloy chemistry amongst other factors. During PBF-AM process it must be low enough to allow the molten metal to spread over the previous layer if a dense final part is to be realized [1], [20]. Conversely, wettability relies on a combination of dynamic fluid forces, gravitational forces, and adhesion forces overcoming surface tension that would otherwise draw the liquid into a spherical shape to minimize surface energy [15]. It can be hindered by oxide contamination on the surface of previous layer, which can in turn cause defects that are detrimental to final part quality [1], [15]. To reduce the formation of oxides, PBF-AM processes are typically done under a controlled atmosphere [1].

1.1.3 Applied Energy Correlations and Combined Processing Parameters

Due to the large number of interdependent processing parameters, PBF-AM processes are typically optimized by combining multiple parameters into expressions to assess the trade-offs between them. Many of these expressions are described in terms of energy applied to the powder bed as it fundamentally governs melt pool formation and the characteristics thereof [15]. They are therefore called Applied Energy Correlations [15]. Most AECs do not take into account all of the relevant parameters, as they are typically based on simplified models of the process [15].

The Andrews Number (E_A) is one of the simplest AECs, as it only considers laser power scan speed and hatch spacing [15]. The most commonly used AEC is the Volumetric Energy Density (E_v, Jmm^{-3}) [20], [21], which is shown Table 1. It is defined at the amount of energy delivered to the powder per unit volume of powder. Unlike Andrew's Number, the Volumetric Energy Density also considers the layer thickness.

An overview of the aforementioned AECs together with others that have been utilized in PBF-AM are shown in Table 1. Again, it should be noted that none of these expressions consider every pertinent variable and are instead used to quickly characterize the influence of the processing parameters in question.

Table 1. Applied energy correlations and relevant processing parameters [20].

AEC (Units)	Definition	Expression	Parameters (Units)
Andrew's Number, E_A (Jmm^{-2})	Energy applied to the powder bed per unit area	$E_A = \dfrac{P}{v \cdot h}$	P: Power (W) v: Scan Speed (mms^{-1}) h: Hatch Spacing (mm)
Volumetric Energy Density, E_v (Jmm^{-2})	Energy per unit volume applied to the powder bed	$E_v = \dfrac{P}{v \cdot h \cdot t}$	P: Power (W) v: Scan Speed (mms^{-1}) h: Hatch Spacing (mm) t: Layer Thickness (mm)
Surface Energy Density, E_s (Jmm^{-2})	Energy applied to the powder bed per unit area scanned	$E_s = \dfrac{P}{v \cdot d}$	P: Power (W) v: Scan Speed (mms^{-1}) d: Spot Size (mm)
Linear Energy Density, E_L (Jmm^{-1})	Ratio of power input to scan speed	$E_L = \dfrac{P}{v}$	P: Power (W) v: Scan Speed (mms^{-1})
Optimal Hatch Spacing, h (mm)	Optimum hatch spacing at the beam waist	$h = 0.7 \cdot w$	w: Beam width at waist (mm)

1.2   Solidification

Solidification describes the phase transformation of matter from liquid to solid. During the solidification of metallic alloys, a crystalline solid is typically formed. As this solid phase grows, differences in the solubility of alloying solutes in the solid and liquid phases causes a compositional gradient to form in the liquid at the solid-liquid interface [13], [24]. This is referred to as segregation and results in local changes to melt and solid-liquid interface properties that can heavily influence the solidified microstructure and defects present.

1.2.1   Segregation and Solute Distribution

The distribution of solute present in the as-solidified microstructure can be roughly approximated using an equilibrium phase diagram, like that shown in Figure 4. At a given

temperature (T), the equilibrium composition of the solid (C_S) and liquid (C_L) can be determined from the liquidus and solidus lines, respectively. The ratio of solute content in the solid to that in the liquid is known as the partitioning coefficient (k) defined as [13], [24]:

$$k = \frac{C_S}{C_L}$$ 1)

k is less than 1 in systems for which solute is segregated to the liquid (Figure 4), and greater than 1 in systems where the first solid formed is solute-rich. As an alloy containing a solute concentration of C_o is cooled just below the liquidus temperature (T_L), the first solid formed will have a composition of $C_s = kC_o$. This is because the composition of the liquid is initially equal to that of the alloy. Subsequently, the composition of the bulk solid is equal to kC_L.

It should be noted that use of the equilibrium phase diagram inherently assumes equilibrium solidification. By extension, this entails full homogenization of both the liquid and solid phases during solidification via solute diffusion and yields a homogenous composition C_o. Practically, this requires extremely low solidification rates and long solidification times that are not characteristic of most industrial solidification practices [13], [24], PBF-AM included. If full homogenization of the solid is not attained, excess solute will be segregated to the liquid as dictated by the partitioning coefficient (i.e. $C_L = C_S/k$) [13], [24]. In turn, a solute-rich boundary layer is formed just ahead of the solid-liquid interface and predictions made by the equilibrium phase diagram are rendered inaccurate. Instead, the Gulliver-Scheil model can be used in lieu of the phase diagram to predict the profile of the solute gradient under conditions where no solid diffusion takes place [13], [24], while models such as the Brody-Fleming model or Clyne-Kurz model may be used under conditions conducive to partial diffusion in the solid [24]. Although consideration of solute profiles can be useful in identifying segregation and compositional

gradients in the solid, they can be further complicated by the morphology of the solid-liquid interface.
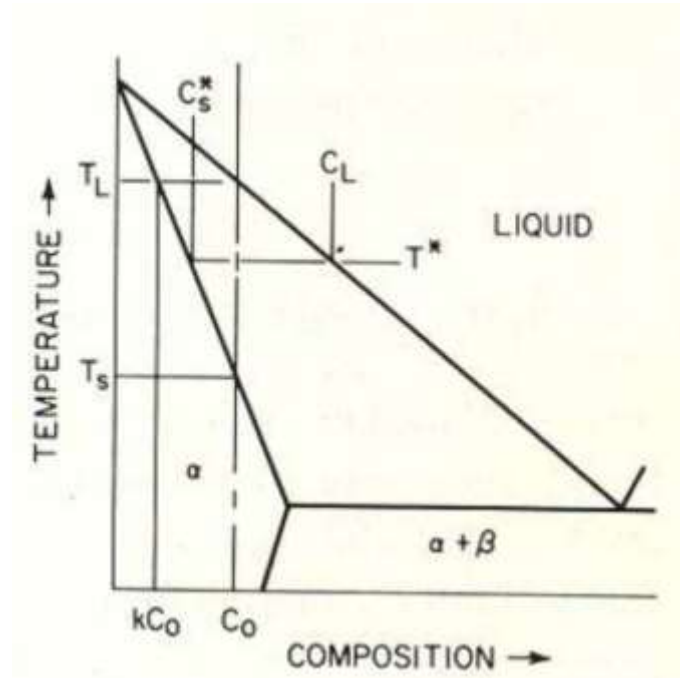
Figure 4. Hypothetical binary eutectic phase diagram showing the relationships between partitioning coefficient and solute content of the solid and liquid phases during solidification [13].

1.2.2 The Solid-Liquid Interface and Microstructure Development

The morphology of the solid-liquid interface dictates the microstructure obtained from a solidification process. The first solid is often formed by heterogeneous nucleation, and proceeds to grow into the liquid with a planar solid-liquid interface (Figure 5 (a)), producing a columnar microstructure. Segregation of solute ahead of the interface then forms not only a local compositional gradient, but a local T_S gradient as well. This is because T_S of a liquid is dependent on composition. If the thermal gradient (G) in the solute-rich liquid results in an actual liquid temperature (T_q) below the local T_S, the liquid is said to be constitutionally undercooled. This is a metastable state and therefore increase in the

14

driving force for solidification. In turn, the growth rate of the solid phase (R), also called the solidification front velocity (SFV), will increase to compensate.

Constitutional undercooling is not uniform across the interface, as minute variation in boundary layer solute concentration exist intrinsically. Therefore, some regions of the interface will grow into the melt more quickly than others and begin to segregate solute both parallel and perpendicular to the solid-liquid interface. This, as well as complex surface tension effects related to the curvature of these regions may then cause them to repeat at regular intervals. These repeating regions are referred to as perturbations.

Depending on the solidification conditions, perturbations may continue to extend into the liquid and ultimately cause the planar interface to break down into cellular interface (Figure 5 (b)). Perturbations may then develop on the surface of the cells, resulting in a further interface breakdown from a cellular morphology to dendritic (Figure 5 (c)).

Furthermore, if constitutional undercooling is sufficient, homogenous nucleation may become kinetically favourable to heterogenous nucleation. The resulting nuclei will then proceed to grow radially, typically with a dendritic morphology, in turn producing an equiaxed dendritic microstructure (Figure 5 (d)). The resultant microstructure is highly dependent on SFV and G in that morphology is dictated by *G/SFV* while the size is determined by *G* x *SFV* (Figure 6) [25].
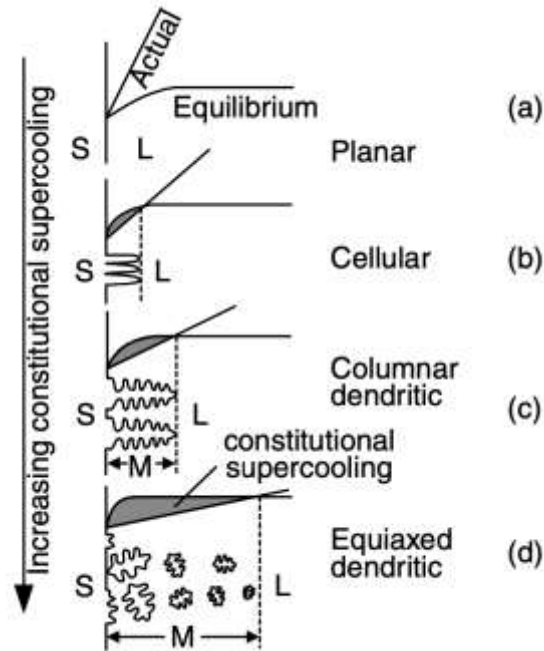
Figure 5. The effects of thermal gradient and temperature at the solid-liquid interface on constitutional supercooling and the resulting morphology [25].
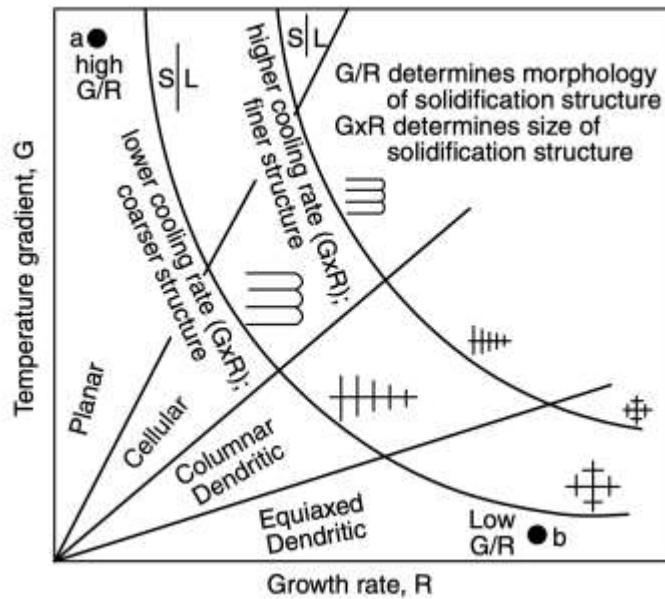
Figure 6. The combined effects of growth rate (SFV) and thermal gradient on morphology and size of the solidification microstructure [25].

1.2.3   Rapid Solidification

It is important to note that constitutional supercooling theory and partitioning coefficients determined using the equilibrium phase diagram are only applicable in solidification-based processes having a low SFV. However, those observed in PBF-AM are typically between 0.1 ms^{-1} and 5 ms^{-1} [26]. As such, PBF-AM is deemed to be a rapid solidification process (RSP). Solidification under these conditions is known to form non-equilibrium microstructures featuring supersaturation and metastable phases [27]–[29].

The supersaturation of solute takes place when the SFV approaches the speed at which solute atoms diffuse through the solid-liquid interface [11], [30], [31]. The fast-moving interface will engulf solute and enrich the solid phase above the equilibrium solute value [11], [30], [31]. This is called solute trapping and causes k to deviate from equilibrium and trend towards unity. If the SFV exceeds the diffusive speed of the solute (v_D), it will be completely trapped, resulting partionless solidification (i.e no solute segregation) and a k value of unity [11], [30], [31].

The Continuous Growth Model derived by Aziz and Kaplan shows the relationship between k_{eq}, SFV, and v_D and can be used to estimate a SFV-dependent partitioning coefficient (k^v) [31]. However, direct measurement of v_D is often impractical, if not impossible. Instead, it can be reasonably approximated as the ratio of the interatomic distance (a_o) to the liquid diffusivity of the solute species (D_L) [11]:

$$k^v = \frac{k_{eq} + \left(SFV/v_D\right)}{1 + \left(SFV/v_D\right)} \cong \frac{k_{eq} + \left(SFV \cdot a_o/D_L\right)}{1 + \left(SFV \cdot a_o/D_L\right)} \qquad\qquad 2)$$

It should be mentioned that the departure of segregation phenomenon from equilibrium is not the only influencing factor on interface morphology during RSP. For example, at high SFVs a planar interface may be stabilized by surface tension [28], [29], [32]. While microstructural development and interface stability during RSP can be explained using the

17

Kurz-Giovanola-Trivedi model [28], further consideration is outside the scope of this work.

1.3 Aluminum Alloys and Aluminum-Based PBF-AM

Aluminum alloys are the second most used in the metals industry, behind ferrous alloys [33]. The widespread use of Al can be attributed to the attainability of unique combinations of properties. The high strength-to-weight ratio of Al alloys is an attractive property in many applications, however they also have excellent corrosion resistance, as well as good electrical and thermal conductivity [33].

The widespread use of aluminum, especially in the transport industry, makes it an attractive candidate for AM, as AM technologies allow near-net-shape, single piece parts with complex geometries to be manufactured [4], [21]. This allows the high strength-to-weight ratio of Al alloys to be fully exploited through the use of hollow-shell or lattice structures to further reduce weight [4]. Historically, many Al products are produced by casting, rendering these weight-reducing structural features was practically impossible to produce [4]. The use of Al in heat management applications could also be drastically improved upon as the use of AM processing can give designers the ability to include conformal cooling channels [4].

With the rise of AM, many alloys that are known to be difficult or costly to process conventionally [21], such as Ni superalloys, Ti-6Al-4V, CoCr alloys, and stainless steels [34] have been heavily researched to improve manufacturing efficiency. While AM could also improve efficiency when processing Al alloys, it has been much less extensively studied. This is because the cost of producing Al parts by conventional means is lower relative to the aforementioned materials [4], [21], despite the opportunities for novel alloy development afforded by the non-equilibrium nature of many AM processes.

1.3.1   Properties of Aluminum Alloys Relevant to Laser Additive Manufacturing

Aluminum alloys that are compatible with PBF-AM are typically based on wrought, weldable chemistries [4], [21]. Many properties of Al alloys influence the weldability, including the presence of an oxide layer, thermal conductivity, coefficient of thermal expansion (CTE), and solidification shrinkage, as well as high hydrogen solubility in the melt [4]. While all are relevant to wire and foil-based AM processes, PBF-AM processes are powder-based and done in an inert atmosphere. Therefore, oxide layer, thermal conductivity, thermal and solidification shrinkages, solidification range and laser absorptivity are most critical to the processability of Al alloys via PBF-AM [4].

The presence of an oxide layer on the surface of any base metal affects weldability significantly [4], [8], [21]. In the context of Al, the oxide layer is composed mainly of alumina (Al_2O_3) and is known to destabilize the melt pool and decrease wettability [4], [8], [21]. It also has a much greater melting temperature than metallic Al (approximately 2050˚C) and as such, will typically remain melted during PBF-AM processes. This is problematic as unmelted oxide inclusions are known to give rise to porosity upon solidification and can act as crack nucleation sites in service [4].

The significant thermal conductivity of Al also influences weldability [4], [8], [21] as it is approximately six times that of Fe [8]. Accordingly Al PBF-AM, the incident laser energy required is frequently greater than that used for ferrous alloys, even though the melting temperature of Al is less than half that of Fe [4], [8]. This can be problematic, as increased laser power is associated with the loss of volatile alloying elements, poor interlayer fusion and defects such as balling [4], [21].

The CTE of Al is also relatively high (24×10^{-6} /˚C) - double that of mild steels (11.7×10^{-6} /˚C). This makes Al especially vulnerable to the formation of residual stresses and concomitant effects such as warping and cracking [8], [35], [36]. Additionally, many Al alloys also experience significant shrinkage during solidification, sometimes greater than

6% by volume in welds [4], [8]. The combination these attributes makes many Al alloys highly susceptible to solidification cracking [35].

Solidification cracks are formed when liquid in the mushy zone is trapped in interdendritic channels or between impinging grains that cannot be fed with additional liquid from the bulk. As temperature and liquid fraction decrease, solidification and thermal shrinkage cause the liquid to contract. Without adequate feeding from the liquid bulk, these shrinkages give rise to stresses along the channels. If sufficient stress is present in the terminal stages of solidification when only a thin liquid film is present, the film will tear, leaving cracks in the solidified microstructure. Additionally, the tensile strength and ductility of Al alloys are typically low in the mushy zone, making them even more susceptible to solidification cracking [35].

Solidification cracking is also related to the solidification range of an alloy, and is dependant mainly on alloy chemistry [8]. Alloys with a large solidification range are particularly prone to solidification cracking [3], [8], [14], [21], [37], [38], as the accumulated thermal strain necessary to form solidification cracks is proportional to the temperature range over which the alloy solidifies [8]. The change in solidification range per percent alloying addition in a binary alloy can be quantified using the relative potency factor (RPF) [8]:

$$RPF = \frac{m_L(k-1)}{k} \qquad \text{3)}$$

Where m_L is the slope of the liquidus line on the phase diagram, and k is the partitioning coefficient.

As previously stated, the poor absorptivity Al is often can be problematic in PBF-AM [4], [21]. When a material is struck with electromagnetic radiation, the incident energy can be transmitted through, reflected, or absorbed by the material (Figure 7) [39], [40].
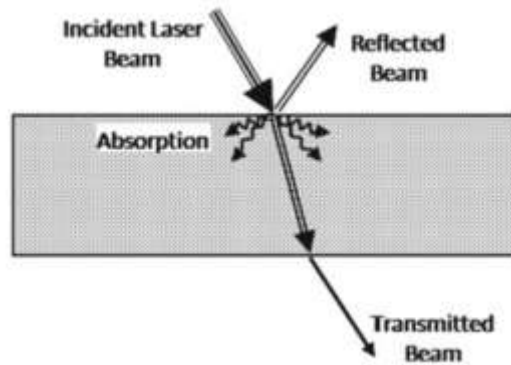
Figure 7. Illustration showing the reflection, absorption and transmission of a laser beam incident on a solid material [39].

The sum of absorptivity (A), reflectivity (R), and transmissivity (T) is equal to unity. However, for opaque solid such as metals, transmissivity is equal to zero, therefore meaning absorptivity and reflectivity are complementary [39], [40]:

$$R + A + T = 1 \qquad\qquad 4)$$

Absorption begins as photons strikes a solid and their electric and magnetic fields interact with those of the electrons in the valence/conduction band of atoms within the solid [39]. If the energy of the incident photons is large enough, electrons are ejected from the solid, leading to the photoelectric effect [39]. However, the lasers used in PBF-AM typically do not produce photons with energy sufficient for electron ejection [39]. Therefore, if electrons are not ejected, interaction with photons excites them into an unstable, high-energy state [39], [40]. Consequently, in order to return to a stable low-energy state, excited electrons will either re-radiate excess energy or will be restrained by the bonding energy of the solid (i.e. lattice phonons) [40]. Re-radiation constitutes reflection or transmission, while restraint by lattice phonons causes the lattice to vibrate, effectively resulting in an increase in temperature [40].

Metals are known to have poor absorptivity of laser energy [8], [21], [36], [39]. This is because electrons in metallically bonded solids are in an "electron sea" and are more free to oscillate and re-emit without interacting with the lattice compared to nucleus-bound electrons in covalent and ionic bonds [40].

Absorptivity, however, is also dependent on wavelength and temperature (Figure 8). At low wavelengths, the material is bombarded with higher energy photons that are more readily absorbed [40]. Conversely, as temperature is increased the number of photons present also increases, which promotes electron-photon interactions [39], [40]. Therefore, more opportunities are present for excited electrons to interact with the lattice rather than re-emit absorbed photon energy, thus increasing absorptivity [39], [40].
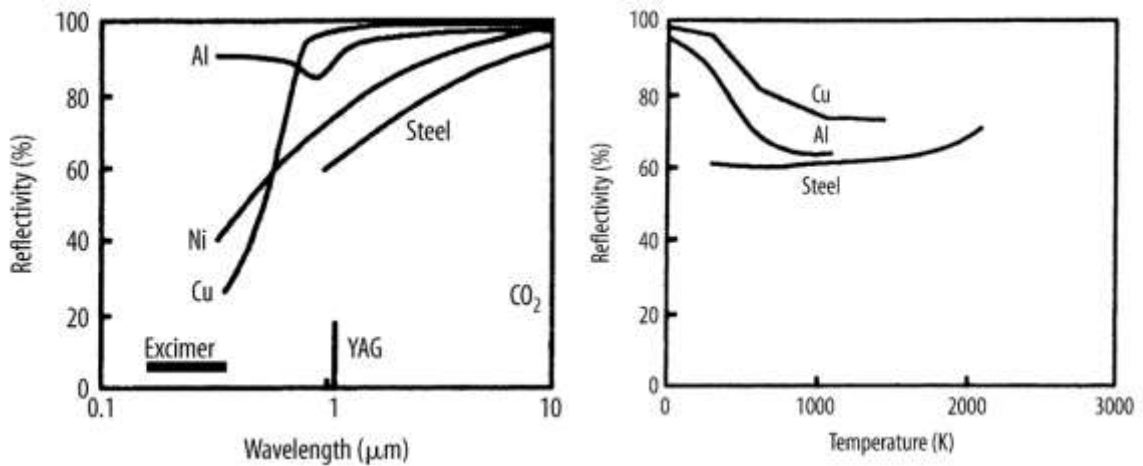
Figure 8. Reflectivity of common metals as a function of wavelength (left) and temperature (right) [40].

1.3.2 Classification and Properties of Aluminum Alloys

Aluminum alloys are classified as either wrought or casting alloys and are identified by a numerical code (Table 2). Wrought alloys are identified using a four-digit designation system (XXXX) where the first digit identifies the alloy series and the last three identify the alloy or the purity of the aluminum [33]. Conversely, casting alloys use a three-digit

system with a fourth digit separated by a comma or point (XXX.X). As with wrought alloys, the first digit identifies the alloy series and the last two digits identify the alloy or purity of the aluminum [33]. The separated digit is used to indicate the product form (i.e. casting or ingot). Casting alloy designations may also be preceded by a letter to indicate a modification of the original alloy chemistry [33].

Table 2. Designation of wrought and casting aluminum alloys [33], [41].

Wrought		Casting	
Designation	*Alloying Elements*	*Designation*	*Alloying Elements*
1XXX	≥99.00% Al	1XX.X	≥99.00% Al
2XXX	Al-Cu	2XX.X	Al-Cu
3XXX	Al-Mn	3XX.X	Al-Si-(Cu,Mg)
4XXX	Al-Si	4XX.X	Al-Si
5XXX	Al-Mg	5XX.X	Al-Mg
6XXX	Al-Mg-Si	6XX.X	Unused
7XXX	Al-Zn	7XX.X	Al-Zn
8XXX	Al-Other	8XX.X	Al-Sn
9XXX	Unused	9XX.X	Al-Other

1.3.2.1 Properties of Wrought Aluminum Alloys

Wrought alloys are further subdivided into those that are heat treatable and non-heat treatable [21]. Non-heat treatable alloys can be strengthened by forming a solid solution, the presence of secondary dispersoid phases, and strain hardening [41]. 1XXX, 3XXX and 5XXX series alloys containing Mg, Mn, and Cr, as well as 4XXX series alloys containing only Si are all considered non-heat treatable [41]. 5XXX series Al-Mg alloys with 0.5-6% Mg are the most used solid solution strengthened alloys, although they are also commonly strain hardened [41]. They are often alloyed with transition elements (Cr, Mn, Zr) to

23

control the grain structure and often contain Si and Fe impurities that form intermetallic dispersoid particles [41].

Al alloys strengthened by the formation of secondary phases are commonly alloyed with elements that have low solid solubility in Al, such as Fe, Ni, Ti, Mn and Cr [41]. These additions often form irregularly shaped intermetallics at the grain boundaries and between dendrite arms upon heating which increase strength and hardness while decreasing ductility [41]. Dispersoids may also refine the microstructure of non-heat treatable wrought Al alloys [41]. Mn and Cr additions are commonly used to achieve a refined grain structure, as they form complex precipitates, such as $Al_{12}(Fe,Mn)_3Si$, $Al_{20}Cu_2Mn_3$, or $Al_{12}Mg_2Cr$ [41]. It is worth noting that these phases do not cause appreciable hardening as they are incoherent with the matrix, and their presence causes a loss in solid solution strengthening. Rather, they inhibit recrystallization and grain growth during subsequent heating [41].

Strain hardening is a highly effective strengthening mechanism for non-heat treatable wrought Al alloys, and results in increased strength, but is also associated with a loss in ductility [41]. In the context of forming operations, it is usually advantageous to use partially annealed feedstock, as they have greater formability for the same strength levels than unannealed materials [41].

Heat treatable or so-called "precipitation hardenable" wrought Al-alloys, are strengthened by the precipitation of small clusters of solute atoms and/or secondary phase(s) [41]. The most widely used alloys of this type are members of the 2XXX, 6XXX and 7XXX series [41]. Precipitation hardening itself relies on the inclusion of additions that have a particular trend of solid solubility in Al. Specifically, an elevated solid solubility at high temperatures that then decreases dramatically with decreasing temperature. The first stage of heat treatment is solutionizing. Here, the product is heated and then held at an elevated temperature where only a solid solution exists. In the case of Al-4 wt.% Cu, (Figure 9 (1)), the alloy would be heated to a temperature between 500 and 580˚C and held to allow a Al-Cu single-phase solid solution to form [33]. Once solutionized, the alloy is quenched to

24

room temperature (Figure 9 (2)) [33]. The rapid cooling curtails the diffusion of atoms necessary to form a second phase. Instead a metastable supersaturated solid solution is formed [33]. The supersaturated solid solution is then aged (Figure 9 (3)), by heating to a temperature into the binary phase field (Al + CuAl$_2$); point 3. This provides the thermal energy necessary precipitate the secondary strengthening phase, in this case CuAl$_2$, in one of several forms that can range from nano-sized coherent clusters to micron-sized incoherent intermetallics [33].
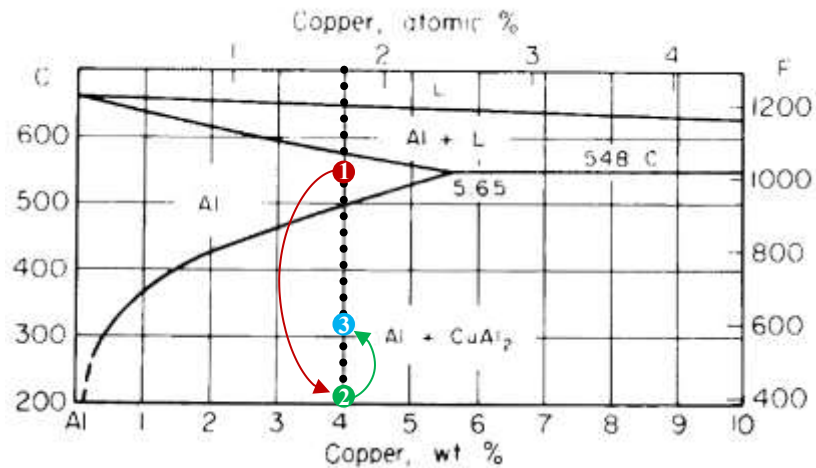
Figure 9. Aluminum-rich region of the aluminum-copper phase diagram illustrating a hypothetical precipitation hardening heat treatment [33].

Aging of precipitation hardenable alloys can be done naturally or artificially. Naturally aged alloys spontaneously form precipitates at room temperature as solute atoms cluster or segregate to select atomic planes within in lattice [41]. The response of an alloy to natural aging is heavily dependent on composition, and is of considerable practical importance [41]. Figure 10 shows that 7075 will never be completely stable, and therefore is hardly used in a naturally aged condition, while 2024 is effectively stable after a few days [41]. Categorically, 2XXX series alloys generally exhibit a feasible response to natural aging [41].
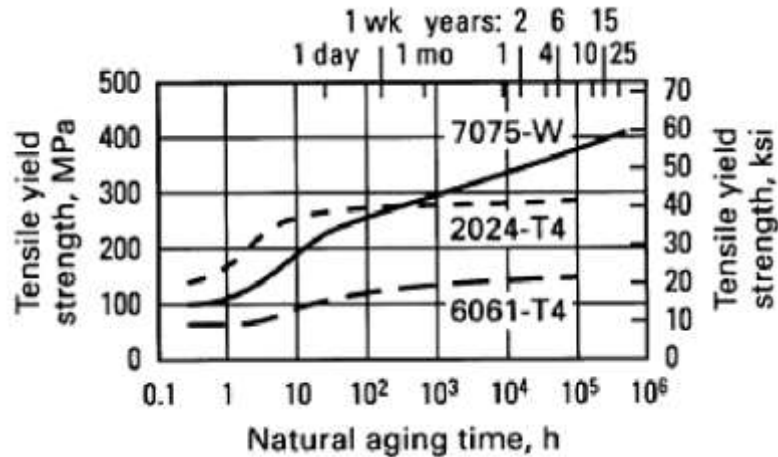
Figure 10. Response of common aluminum alloys natural aging [41].

Artificial aging transpires by heating the as-quenched product above room temperature to produce transitional or metastable forms of the equilibrium precipitates [41] that are often coherent with the matrix. However, excessive aging time or temperature can cause precipitates to transform into the equilibrium phase [41]. This is referred to as over-aging and while it results in a loss in strength, it is sometimes purposely done to improve ductility, thermal stability, or corrosion resistance [41].

The strengthening of an alloy by precipitates arises from the way in which they interact with dislocations as described by Orowan mechanics [42]. Fundamentally, dislocations cannot move through precipitates of sufficient size as they are often strong intermetallic phases. Instead, they will bow around precipitate as they pass within their vicinity (Figure 11 (a)), in turn hindering their motion [42], [43]. However, bowing will continue as stress is applied until a dislocation loop is formed around the precipitate (Figure 11 (b)). These loops are referred to as Orowan dislocation loops, and allow the dislocation to be freed from the pinning action of precipitate [42], [43].
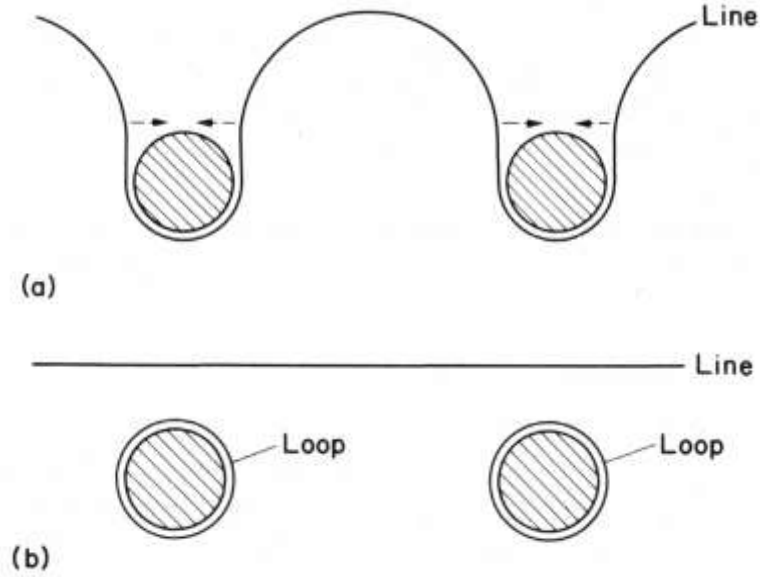
Figure 11. An illustration showing (a) a dislocation bowing around precipitates and (b) Orowan dislocation loops formed around precipitates [44].

The stress required to form Orowan loops (σ_{or}) is observed physically as an increase to the yield stress and is dependent on material properties of the matrix, including the Taylor factor of the matrix (M), the shear modulus (G) and Poission's ration (v) of the matrix, as well as the magnitude of the Burger's vector (b), the mean planar precipitate radius ($\bar{R}$), and the effective interparticle distance (λ) [42]:

$$\sigma_{or} = M \cdot \frac{0.4Gb}{\pi\sqrt{1-v}} \cdot \frac{\ln\left(\frac{2\bar{R}}{b}\right)}{\lambda} \qquad 5)$$

It is worth noting that the above expression assumes the precipitates to be incoherent [42]. Coherent precipitates further increase strength as the associated reduction in the lattice parameter mismatch between the matrix and precipitate causes the development of a strain field in the lattice that inhibits dislocation climb [42].

Additionally, $\bar{R}$ is not the mean precipitate radius, and is inversely proportional to it [42]. Therefore, as precipitate size increases the stress required to form Orowan loops decreases [42]. σ_{or} is also dependent on the volume fraction of the precipitate phase, as λ decreases with increasing volume fraction of precipitates. However, in Al alloys where precipitates are formed by alloying additions with low solid diffusivity and solubility in Al, the attainable volume fraction is often limited [42]. Therefore, adequate strengthening in such alloys often requires extremely fine dispersoids, sometimes on the order of 10 nm in size [42].

1.3.2.2   Properties of Aluminum Casting Alloys

Aluminum casting alloys are commonly seen as the most versatile of all foundry alloys, as they are among the most castable [41]. Their excellent castability is largely attributable to their good fluidity, low melting points, low susceptibility to solidification cracking and hot tears, as well as good chemical stability [41].

4XX.X series Al-Si casting alloys are used where good castability and corrosion resistance are required [41]. They typically contain 5-13% Si and have a microstructure consisting of an α-Al matrix containing 1% Si in solid solution together with particles of essentially pure Si; commonly, these phases are coupled as a lamellar eutectic [41]. It is not uncommon for these alloys to have high Si content, as Si greatly improves fluidity and lowers coefficient of thermal expansion. At Si contents above 12-13%, primary Si crystals are present in the microstructure that can drastically improve wear resistance [41]. Small Mg additions are also common when high strength and hardness are required and can make Al-Si alloys heat treatable [41].

In foundry settings, the most widely used Al casting alloys are the 3XX.X series, specifically Al-Si-Cu alloys [41]. While Al-Cu casting alloys are of some practical importance, they offer relatively poor castability and have therefore been largely replaced by Al-Si-Cu alloys [41]. As with Cu-containing wrought alloys, Al-Si-Cu alloys containing more than 3-4% Cu are heat treatable [41]. However, precipitation hardening heat

treatments are usually used only for alloys that also contain Mg, as it intensifies age hardening behavior [41].

1.3.3   Thermal Stability of Aluminum Alloys

As previously stated, conventional high-strength Al alloys are typically strengthened by the formation of second-phase precipitates upon aging of a super saturated solid solution [8], [41]. This input of thermal energy causes small clusters of alloying element atoms or second phase structures to form by diffusion processes [41]. Once formed, these precipitates impede the motion of dislocations through the lattice, improving strength [8]. However, if exposure to elevated temperatures is prolonged, precipitates will inevitably coarsen, and possibly even dissolve [41], [42], [45]. Such transitions deteriorate the efficacy of this strengthening mechanism and invoke a dynamic loss in mechanical properties. Therefore, it is imperative that any alloy exposed to elevated temperatures in service be resistant to these microstructural changes [8], [42].

In precipitation strengthened alloys, coarsening of precipitates through Ostwald ripening is especially problematic, as large, sparsely distributed precipitates strengthen much less effectively than fine, well dispersed ones [8], [42]. Ostwald ripening is the growth of larger precipitates at the expense of smaller ones, and is driven by a reduction in interfacial energy (σ) between the matrix phase and precipitates [46]. Interfacial energy is largely dependent on the curvature of the interface, and therefore the precipitate radius (R) [46]. However, Ostwald ripening is also a time (t) dependent process and the extent of this effect can be calculated as per equation (6) and is schematically illustrated in Figure 12:

$$R_t^3 - R_O^3 = kt \qquad\qquad 6)$$

Where the change in precipitate radius after some time (R_t) relative to the initial radius (R_O) caused by Ostwald ripening is determined by a rate constant (k). It is also proportional

to σ, as well as the diffusivity of the rate-limiting solute (D), and the equilibrium solubilities of the solute in the matrix phase (C_e^α) and precipite phases (C_e^β):

$$k \propto \frac{D\sigma}{\left(C_e^\beta - C_e^\alpha\right)^2} \qquad\qquad 7)$$
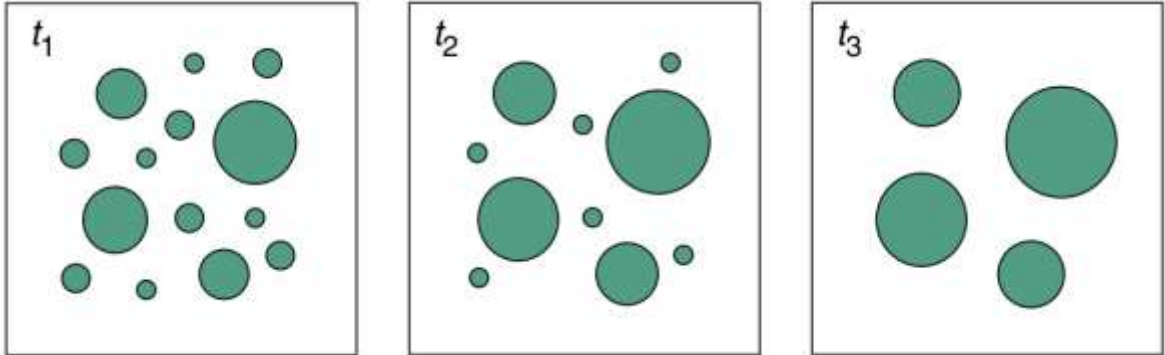
Figure 12. Illustration showing the growth of large precipitates at the expense of smaller ones over time due to Ostwald ripening ($t_1 < t_2 < t_3$) [47].

Given the aforementioned limitations on precipitate stability, thermal stability is commonly achieved in aluminum alloys by engineering the microstructure such that it contains intermetallic dispersoids formed from elements having low solid solubility and diffusivity in α-Al, as these attributes ensure minimal growth at elevated temperatures [8], [42], [45], [48], [49].

For service at elevated temperatures, ideal dispersoid phases must be thermodynamically stable and coherent to the matrix to prevent dissolution and restrict dislocation movement, respectively [50]. When the strengthening mechanisms and the kinetics of dispersoid stability are considered, 3 criteria for viable alloying additions in this context can be stated [8], [42], [45], [49]:

1. *Alloying additions must be able to form a stable, strengthening phase in an Al-based alloy.*

The dispersoids formed must be of sufficient volume fraction, thermodynamically stable at elevated temperatures, resistant to shearing by dislocations, of a desirable morphology, and possess a crystal structure with minimal lattice mismatch relative to the α-Al matrix.

2. *Alloying additions must have a low diffusivity in Al, especially at elevated temperatures.*

Low diffusivity of the alloying addition in the α-Al matrix limits diffusion-dependent coarsening of the dispersoid phase.

3. *Alloying additions must have a low solubility in Al, especially at high temperatures.*

Low solubility of the alloying addition in the α-Al matrix limits dissolution of the associated dispersoid phase.

Transition metal (TM) trialuminide intermetallics (Al_3M) are viable candidates as dispersoids, as they are often the most Al-rich intermetallic phase. They also have low density, high specific strength, good thermal stability, and excellent corrosion resistance [42]. Many TMs have low diffusivity and solid solubility in the α-Al matrix (Table 3) [8], [42], [45], [49] and often have crystal structures that are coherent or semi-coherent with the Al matrix [42], [50].

Table 3. Maximum solubility and diffusivity of select transition metals in α-Al [48].

Element	Maximum solubility (at%)	Diffusivity at 427°C (at%cm^{2}s^{-1})
Ti	0.8	3.86×10^{-15}
V	0.2	3.94×10^{-15}
Cr	0.42	2.3×10^{-14}
Fe	0.026	1.12×10^{-15}
Ni	0.023	8.4×10^{-15}
Zr	0.07	6.6×10^{-17}
Nb	0.065	1.9×10^{-14}
Mo	0.07	6.03×10^{-15}

The late period IV elements Fe and Ni are two such TMs [42]. In fact, many existing thermally-stable Al alloys are based on the hypereutectic Al-Fe system (Figure 13) and often contain ternary and quaternary additions and/or rare earth metals (REMs) such as Ce

(Table 4) [8]. Under equilibrium solidification conditions, Al-rich Al-Fe alloys form $Al_{13}Fe_4$ (Al_3Fe), an incoherent intermetallic with a base-centered monoclinic structure [8], [51], [52]. The $Al_{13}Fe_4$ phase typically exists as a component in an αAl-Al_3Fe lamellar eutectic, but may also be present as a primary proeutectic phase in hypereutectic alloys, or as discrete precipitates in α-Al that form upon cooling [42]. However, $Al_{13}Fe_4$ is generally coarse and reduces ductility [8]. Therefore, most Al-Fe based alloys have been historically processed via compaction-based powder metallurgy of powders manufactured through rapid solidification techniques such as melt spinning [8], [53].
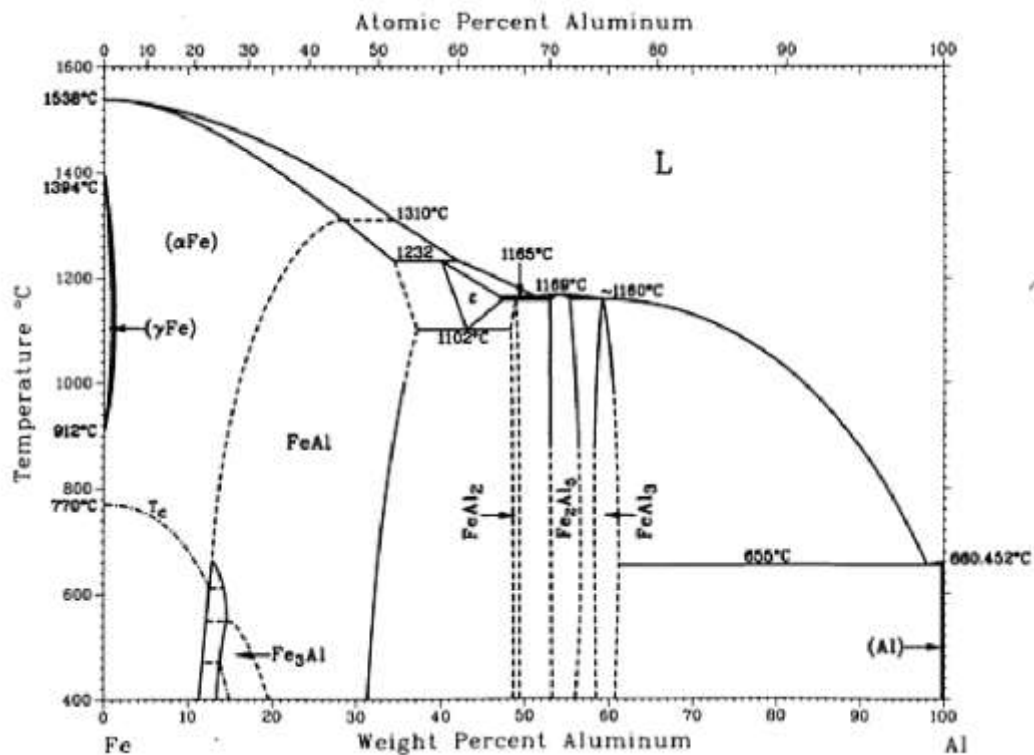
Figure 13. The equilibrium aluminum-iron phase diagram [54].

Table 4. An overview of commercially available dispersion strengthened aluminum-iron alloys [8].

Nominal Composition (Wt.%)	Manufacturer
Al-8Fe-1.7Ni	Alcoa
Al-8.4Fe-3.7Ce	Alcoa
Al-9Fe-4Ce (AA8019)	Alcoa
Al-9Fe-7Ce	Alcoa
Al-10Fe-5Ce	Alcoa
Al-8.5Fe-1.3V-1.7Si (AA8009)	AlliedSignal Inc.
Al-11.7Fe-1.2V-2.4Si (FVS 1212)	AlliedSignal Inc.
Al-8Fe-2.3Mo	Pratt & Whitney

Rapid solidification suppresses the formation of Al_3Fe, instead forming a highly refined αAl-Al_6Fe microeutectic and α-Al supersaturated with Fe [8]. The Al_6Fe phase is metastable and has an orthorhombic crystal structure [54]. Upon subsequent heat treatment, dispersoids of stable, incoherent Al_3Fe as well as metastable semi-coherent Al_9Fe_3 can precipitate from supersaturated α-Al [8], [52], [54]. The Al_9Fe_3 dispersoids tend to have a spherical morphology, which provides good ductility, as well as excellent strength and thermal stability [8].

Ternary and quaternary additions are often added to stabilize the Al_9Fe_3 phase and to form other desirable dispersoid phases [8]. Ce is a common addition that is used to suppress the formation of Al_3Fe, and instead form complex Al-Fe-Ce intermetallics [55]. Commonly, these intermetallic phases can form up to 25-30% of the microstructure by volume, and are distributed both throughout the α-Al matrix and at grain boundaries as shown in Figure 14 [56].

A study into the consolidation of rapidly solidified Al-8Fe-4Ce (wt.%) powder by means of hot forging was completed by Griffith et al [57]. The products demonstrated outstanding

thermal stability such that even after 1000 hours of heating at 450˚F (232˚C), no change in microstructure was observed [57]. In a similar study by Kirchoff et al [55], stable mechanical properties were measured up to 400˚C with exposure times as long as 120 hours. Degradation of mechanical properties at temperatures above 400˚C was observed, and was attributed to the coarsening of intermetallic phases [55].

Vanadium is also a common ternary addition to Al-Fe alloys. Shek et al observed the presence of quasi-crystalline particles in rapidly solidified Al-2Fe-4V and Al-2Fe-8V (wt. %), as well as an amorphous phase [58]. These structures can promote extremely high yield strength on the order of 1400MPa, as well as good ductility and thermal stability [58]. Al-Fe-V alloys are often alloyed with Si as well, since it promotes the formation of the thermally stable $Al_{13.18}(Fe,V)_{1.84}Si$ phase [59] and the presence of a highly refined cellular structure (Figure 15). However, above 3 wt.% Si a Si-rich phase with moderately poor thermal stability may form [59].
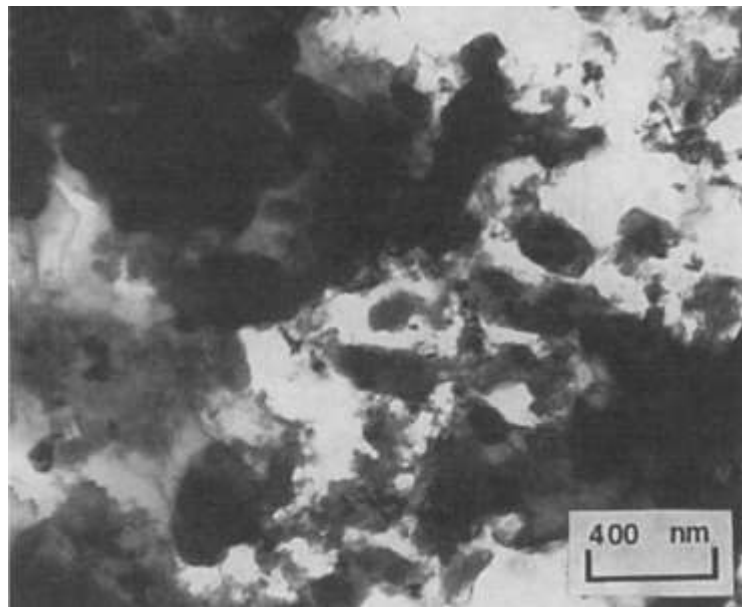
Figure 14. Electron micrograph of rapidly solidified Al-8.4Fe-3.4Ce (wt.%) showing nano-scale intermetallic phases in an α-Al matrix [52].
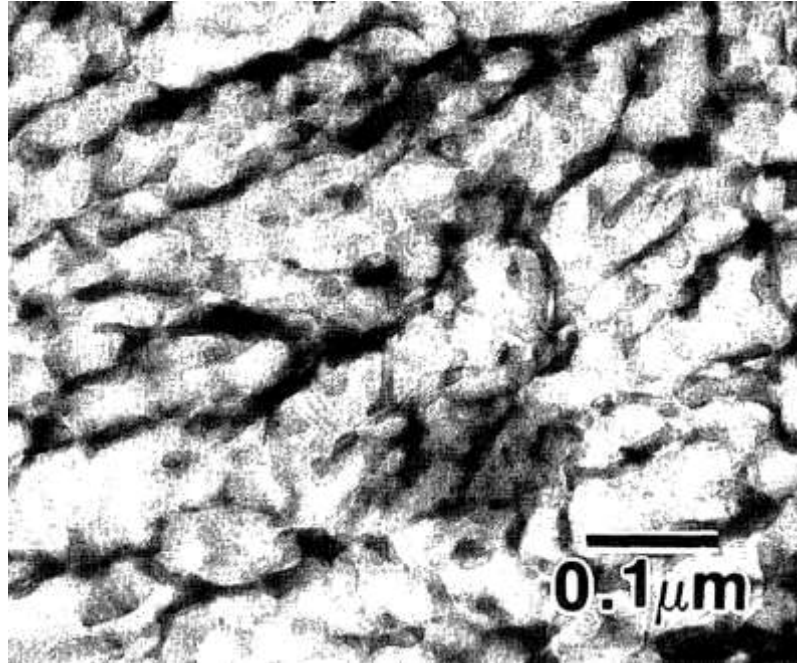
Figure 15. Electron image showing a fine cellular microstructure in a rapidly solidified Al-Fe-V-Si alloy [48].

Al-Ni alloys are also good candidates for applications requiring thermal stability. At equilibrium, Ni has a maximum solid solubility of 0.24 wt.% in α-Al (Figure 16) and is in equilibrium with the orthorhombic structured Al_3Ni phase [54]. The microstructure of cast hypoeutectic (<5.7 wt.%) Al-Ni alloys generally consists of dendritic α-Al with an interdendritic α-Al-Al_3Ni lamellar eutectic containing some discrete Al_3Ni particles [54], [60]. This eutectic is thermally stable and has been reported to resist coarsening up to 500°C [61]. When rapidly solidified, particles of Al_3Ni form mostly at the grain boundaries, but may also be thinly dispersed throughout the matrix [54], [62].
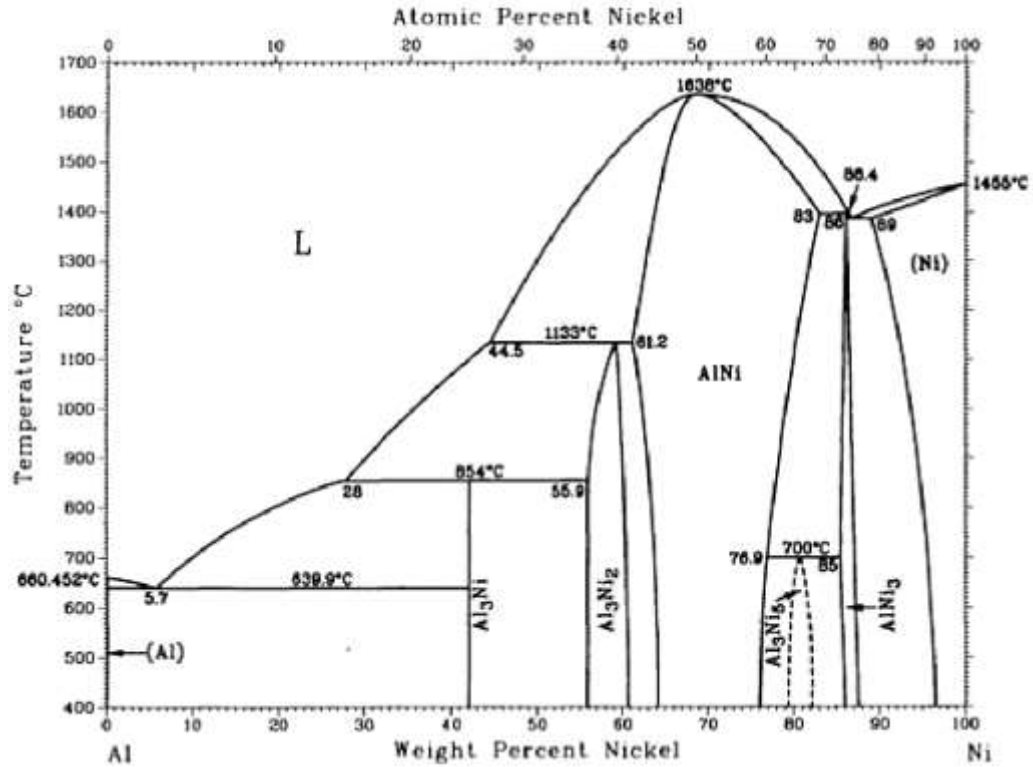
Figure 16. The equilibrium aluminum-nickel phase diagram [54].

1.3.4 Aluminum Alloys Used in Additive Manufacturing

Al-Si and Al-Si-Mg casting alloys are among the Al-based alloys most commonly researched for use in AM, as they have exhibited a desirable processing response in light of their high fluidity and low solidification shrinkage [4], [21]. Specifically, eutectic Al-12Si and AlSi10Mg have small solidification temperature ranges compared to conventional wrought alloys such as 7075 and 6061 (Figure 17) and are therefore of particular research interest [4], [21].

Al-Si alloys with Si contents as high as 20% have also been investigated [21]. The microstructure is relatively similar to that of Al-12Si, although some supersaturation of Si in the Al matrix has been observed [21]. A reduction of Si is known to increase the solidification temperature range and Al-Si alloys below 4% Si were found to be prone to solidification cracking [21].
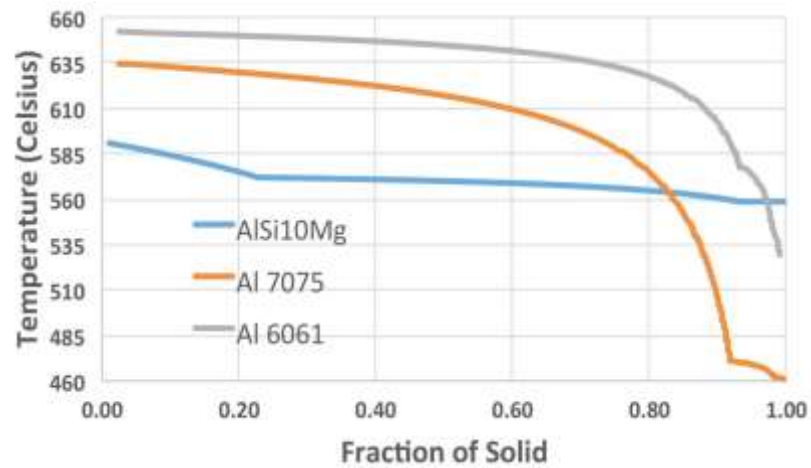
Figure 17. The solidification ranges of select aluminum alloys [26]

When conventionally cast, AlSi10Mg (10wt.% Si and 0.2-0.7 wt.% Mg) typically features a solidified microstructure containing cellular-dendritic Al surrounded by a lamellar eutectic Al-Si phase, as shown in Figure 18 [63]. Metastable Mg_2Si may also be present in alloys containing 0.2 to 0.6% Mg, and can provide strengthening upon precipitation hardening [64]. Similarly, the microstructure of conventionally cast eutectic Al-12Si consists of intergranular acicular Si or lamellar eutectic Al-Si structures throughout an α-Al matrix [65].
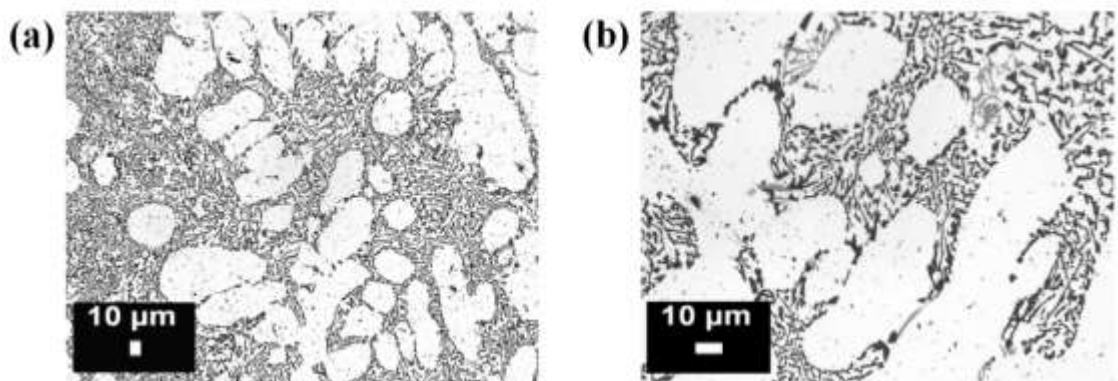
Figure 18. Micrograph showing the cellular structure of α-Al and Al-Si eutectic in cast AlSi10Mg at (a) low magnification and (b) high magnification [63]

When such alloys are processed by PBF-AM drastic microstructural changes are noted because of the exceptionally high cooling rates involved. AlSi10Mg has an extremely refined cellular-dendritic Al microstructure surrounded by the same lamellar eutectic Al-Si phase, with a small amount Mg_2Si (Figure 19) [63], [64]. Lam et. Al showed the average size of the Al cells in as-printed AlSi10Mg to be 500 nm compared to 360 μm for an as-cast sample. The refined microstructure resulted in an average microhardness value of 123 HV [64]. The presence of Mg_2Si was confirmed via XRD and was assumed to be the cause of high Mg contents of 10.84-12.55% in the eutectic structure relative to the bulk content of 0.2-0.5% [64]. PBF-AM Al-12Si also maintains an extremely fine, cellular microstructure with Si along the cell boundaries [34].
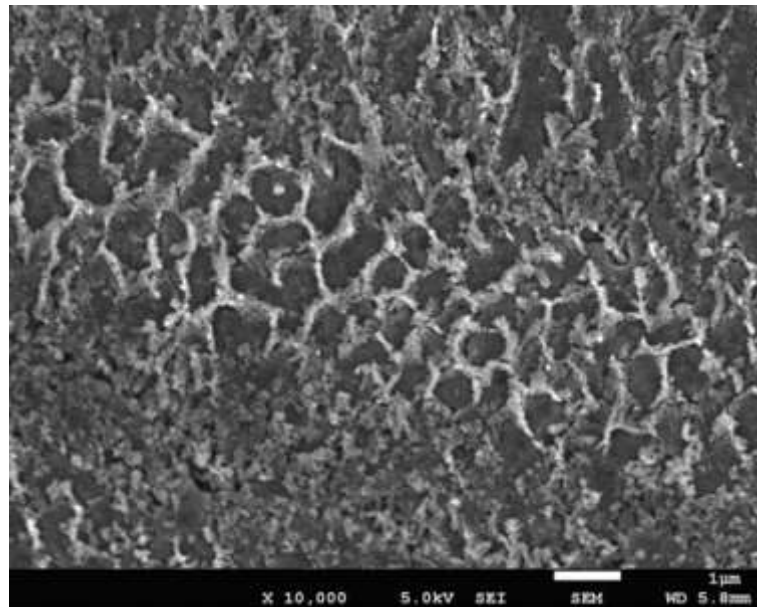
Figure 19. Electron micrograph showing a fine cellular microstructure in AlSi10Mg processed by PBF-AM [64]

The tensile properties of Al-Si alloys in various conditions are presented in Table 5. Here it can be seen that the refined microstructure present in Al-Si alloys processed by PBF-AM is very advantageous [34], as it manifests appreciable gains yield strength without an adverse effect on tensile ductility. Interestingly, post-build heat treatments that would normally invoke additional gains are largely ineffective. Here, the microstructural

coarsening that transpires during heat treatment more than offsets the beneficial effects of precipitate formation such that there is little to no improvement in tensile properties relative to as-built counterparts [34].

Table 5. Tensile properties of aluminum-silicon alloys in various conditions [34]

Alloy	Condition	YS (MPa)	UTS (MPa)	Elongation (%)
Al-12Si	As-cast	130	240	1
	As-built	260	380	3
AlSi10Mg	As-cast	140	240	1
	As-built[1]	230 ± 5	328 ± 4	6.2 ± 0.4
	As-built[2]	240 ± 8	330 ± 4	4.1 ± 0.3
AlSi10Mg	T4	131 ± 9	227 ± 4	6.9 ± 0.8
	T6	245 ± 8	278 ± 2	3.6 ± 0.8

Heat treatable Al alloys present some challenges in PBF-AM as they are often prone to solidification cracking [4], [21]. Each of these alloys has a specific solute content range in which the thin liquid film necessary for solidification cracking will form, called the crack sensitivity range [4]. Therefore, any alloy having solute contents within this range are said to be unweldable and not applicable to AM [4]. Despite this, some heat treatable Al alloys have been successfully processed [4], [21], [34]. For example, the 2XXX series alloy AA2219 has been successfully processed by wire-fed electron beam freeform AM [4], [21], as the 6% Cu content is above the crack sensitivity range. This, combined with the fast

---

[1] Properties are in the build direction.
[2] Properties are perpendicular to the build direction.

thermal cycles typical of AM processes, resulted in a strongly refined, non-equilibrium microstructure with very little porosity, no cracking, and full interlayer bonding [21].

6XXX and 7XXX series are challenging to process directly, as they are vulnerable to hot cracking and the vaporization of their major alloying constituents [4], [21]. Some work has been done on 6061, however it was shown to be very susceptible to epitaxial growth, as it had large grains that spanned over multiple layers [34]. Martin et al. successfully processed 7075 modified with ZrH_2, who observed a crack-free microstructure of fine, equiaxed grains [26]. This was attributed to the grain refining action of homogenously nucleated Al_3Zr and resulted in mechanical properties comparable to that of wrought 7075 [26].

Al-Mg-Sc alloys are also well known to be viable for PBF-AM [34]. Typically falling under the trade name "Scalmalloy", these systems are highly amenable to PBF-AM and have strength-to-weight ratios comparable to some Ti-based alloys [4] while retaining excellent ductility [4], [21], [34], [36]. It has been reported that their positive processing response stems from the Sc additions that form a refined distribution of the potent grain refiner, Al_3Sc. Even if supersaturated in α-Al after an AM process, subsequent heat treatments result in the precipitation of coherent nano-scale Al_3Sc [4], [21], [34], [36]. The microstructure of these alloys is typically bimodal, with fine equiaxed grains of 100nm-1μm in size at the melt pool boundary and coarser 2-5μm columnar grains towards the melt pool center [34]. The ability to obtain nano-sized grain is largely due to a combination of high cooling rates and the grain refining effects of Al_3Sc [34]. Further modification with Zr is also common as it promotes the formation of $Al_3(Sc,Zr)$; another powerful grain refiner [4]. Hardness values of 80-110 HV and 160 HV have been reported for Al-Mg-Sc-Zr alloys in as-built and post-heat treatment conditions, respectively [4].

The Al-Mg-Zr system has also been recently exploited for use in PBF-AM. Under the trade name Addalloys (NanoAl) the final product is said to be thermally stable up to 350˚C, have post-build densities above 99.5% theoretical, and require only a single-step post-build heat

treatment [66]. The metallurgy of Addalloys is similar to that of Scalmalloys, although they rely on Al_3Zr as a grain refining intermetallic in lieu of Al_3Sc [6], [10], [66], [67].

Another alloy designed specifically for PBF-AM is A20X as developed by Aeromet International. Fundamentally, it is a TiB_2-modified Al-Cu casting alloy that contains 3.0-6.0% Cu, TiB_2 additions of up to 20%, as well as Ti contents up to 1% [68]. While it would be expected that additions of hard, brittle particles such as TiB_2 in such large quantities would diminish mechanical properties, a yield strength of 415 MPa, UTS of 477 MPa, and elongation of 13% have been reported [69]. This is because additions of TiB_2 foster a desirable solidification behaviour that includes grain refinement and the elimination of solidification cracking [68]. During solidification, TiB_2 particles nucleate in interdendritic channels, filling them and blocking the movement of the remaining liquid through them [68]. This causes a shift from liquid feeding to mass feeding in the channels, reducing connected shrinkage porosity [68]. Although TiB_2 is a known grain refiner in Al alloys, grain size can still be as large as 1mm in slow cooled or large castings [68]. Thus, further additions of Ti are included to improve wetting on TiB_2 particles. This allows for further refinement of the microstructure [68], and ultimately improves both processability and mechanical properties.

2   RESEARCH OBJECTIVE

This study was activated as part of a larger, long-term initiative that seeks to develop thermally stable Al alloys specifically for PBF-AM. The central objective of this sub-project seeks to evaluate the effects of Fe and Ni additions on aluminum powder processed in the context of PBF-AM. These TM additions were selected as they are believed to hold considerable promise for commercial exploitation given that they are low cost and are known to invoke positive gains in the thermal stability of wrought aluminum alloys. To produce high quality products, PBF-AM processing parameters were varied in a systematic manner and the builds characterized. Key areas of assessment were the absence/presence of defects, physical property measurements (density, hardness, surface roughness), and microstructure analysis.

3 LASER POWDER BED FUSION PROCESSING OF ALUMINUM POWDERS CONTAINING IRON AND NICKEL ADDITIONS

J. Hierlihy[1], I.W. Donaldson[4], M. Brochu[5], G.A.W. Sweet [3], D.P. Bishop[2]

1 – Graduate Student, Dalhousie University, Halifax, Nova Scotia, Canada
2 – Professor, Materials Engineering, Dalhousie University, Halifax, Nova Scotia, Canada
3 – Postdoctoral Fellow, Dalhousie University, Halifax, Nova Scotia, Canada
4 – Director, Advanced Engineering, GKN Sinter Metals, Conover, North Carolina, USA
5 – Professor, Materials Engineering, McGill University, Montreal, Quebec, Canada

Status: Under review by HI-AM network scientific advisory committee for public release.

The following experimental procedures, results, and discussion were primarily completed by J. Hierlihy. Secondary authors aided in data acquisition/review, manuscript editing, and/or project supervision.

Abstract: The variety of aluminum alloys currently used in laser powder bed fusion additive manufacturing (PBF-AM) is limited, yet the demand for such materials is growing. The AM community is particularly keen on aluminum alloys that offer enhanced thermal stability. Traditionally, this trait has been instilled through transition metal additions that form stable aluminides. This project seeks to devise new PBF-AM materials in this context starting with a precursory study into the effects of iron and nickel additions. Here, gas atomized Al-1Fe and Al-1Ni (wt.%) powders were processed via PBF-AM over a range of volumetric energy densities achieved through systematic adjustments to laser power, scan speed, and hatch spacing. The microstructure (OM, SEM, EDS, XRD) and physical properties (hardness, density, surface roughness) of the products were characterized. Results indicated that Al-1Fe was more responsive to processing as it densified to 99.0% of full theoretical and had a hardness of 95 HRH. Conversely, Al-1Ni only reached 97.8% theoretical density and a peak hardness of 78 HRH. It was also more prone to solidification cracking. Energy density values of at least 32.5 J mm^{-3} were necessary to achieve peak density and hardness.

Keywords: Aluminum, Additive Manufacturing, Thermal Stability, Transition Metals, PBF-AM

3.1   Introduction

Laser powder bed additive manufacturing (PBF-AM) uses laser energy to selectively melt particles in a layer-wise fashion to build a part. It presents unique opportunities for innovation to designers and engineers as it imparts exceptional freedom in component geometry while the highly non-equilibrium nature of the process offers an avenue for the development of novel materials with unique microstructures and properties [1]. A variety of metallic systems are now commercially utilized in PBF-AM including those based on Fe, Ni, Ti, and Al [70]. However, under each of these parent metals there exists but a small handful of alloy chemistries available to end users. For example, only a singular aluminum alloy (AlSi10Mg) utilized in PBF-AM maintains ASTM recognition [2], yet traditional metal forming technologies can choose from over 600. In and of itself, AlSi10Mg performs relatively well in PBF-AM as densities as high as 99.8% theoretical are reported [71]. However, texturing and anisotropic properties are commonly observed as the re-melting of previous layers promotes the epitaxial growth of columnar grains [72]. To address the shortfall in Al-based alloys, the direct application of various commercial wrought alloy chemistries in a PBF-AM context has been attempted and proven to be challenging. Key issues have included solidification cracking and evaporation of volatile constituents [73] given that such alloys were not originally designed for AM.

An emerging area of alloy development in AM is the addition of transition metals (TM) and/or rare earth metals (REM) to Al alloys. This approach has been extensively studied in rapidly solidified Al alloys, wherein the formation of coherent and stable precipitates promotes grain refinement and thermal stability [74]. In certain instances, AM leverages this concept to mitigate the solidification issues encountered with conventional alloys. For example, additions of Zr and/or Sc to Al alloys are well documented to be effective in producing Al_3M precipitates that seed heterogenous nucleation and blunt epitaxial grain

growth. Recent examples include Scamalloy (Al-Mg-Sc) [75] and Addalloy (Al-Mg-Zr; NanoAl) [6]. Furthermore, the relatively low diffusivity of these TM constituents means that they are inherently more thermally stable when compared to conventional aluminum alloying additions [73]. Other attractive TM options are Fe and Ni as these have been exploited for decades in wrought systems such as 2618 (Al-2.3Cu-1.6Mg-1.1Fe-1Ni) and are readily available at low cost. These elements also exhibit low solid solubility in Al, produce stable intermetallic compounds, and exhibit relatively low solid state diffusivity [74]. Accordingly, the objective of this research is to evaluate the applicability of Fe and Ni additions to aluminum processed by PBF-AM. This work was meant to serve as a preliminary investigation on the suitability, physical properties, and microstructure Al-Fe and Al-Ni alloys processed using PBF-AM.

3.2   Materials and Methodology

Two prealloyed aluminum-based powders were employed in this study, alloyed nominally with one weight percent of either nickel (denoted as 'Al-1Ni') or Fe ('Al-1Fe'). Both powders were produced by Kymera International via gas atomization and subsequently classified to a +20/-45 μm cut by sieving. Relevant compositional information measured by inductively coupled plasma – optical emission spectroscopy (ICP-OES) and particle size information measured by laser light scattering (Malvern Mastersizer 3000) are shown in Table 6.

Table 6. Measured composition and critical particle sizes of the Al-1Fe and Al-1Ni powders used.

Powder	Composition (wt%)				Particle Size (μm)		
	Al	Cu	Fe	Ni	D_{10}	D_{50}	D_{90}
Al-1Fe	Bal.	0.03	1.08	0.27	19.7	35.3	62.3
Al-1Ni	Bal.	0.17	0.08	0.94	21.3	37.1	64.7

1cm^3 cubed specimen were prepared using an Aconity3D Mini system equipped with a 400W continuous wave Yb-fibre laser ($\lambda = 1070$ nm) that was operated with a fixed beam diameter of 80 μm. Preliminary cubes were hollow specimens prepared by traversing the laser over a single perimeter track during each layer. Others were solid specimens whereby each layer was fabricated using a raster pattern that was rotated 90° between successive layers. All specimens were constructed on heated (220 °C) build plates of wrought 6061-O under an Ar atmosphere ($O_2 < 20$ ppm) and a fixed layer thickness of 30 μm. Process variables included adjustments to the laser power (170 to 190 W), laser raster speed (1000 to 2000 mm/s), and hatch spacing (120 or 150 μm). Select builds were annealed isothermally at 530°C for 4 hours in air and cooled.

Surface characterization was performed using a Keyence VK-X1000 3D laser scanning confocal microscope. Each cube was observed on the as-printed top and side surfaces. Density measurements were performed according to MPIF standard 42 using the 'wet' approach with results normalized using the theoretical maximum density for each material; a value calculated using the inverse rule-of-mixtures approach. Hardness data were captured in the Rockwell "H" scale using a Wilson instruments Rockwell 2000 system. A minimum of 5 measurements were made on each sample with average values plotted. Specimens for metallography were sectioned parallel to the build direction and a side face, mounted in conductive Bakelite, was polished using a standard sequence of SiC papers, diamond suspensions and colloidal silica. Select mounts were etched with Keller's reagent. Optical micrographs were acquired using an Olympus BX51 while energy dispersive x-ray spectroscopy data (15 kV) and electron micrographs were acquired with a Hitachi S-4700 cold field scanning electron microscope. X-ray diffraction was completed using a Bruker D8 Advance operated with Cu Kα radiation generated at a voltage of 40 kV and 20 mA.

3.3 Results

3.3.1 Single-Track

Initially, single track cubes were built to gain a sense of the nominal processing response exhibited by each powder and identify the range of processing conditions suitable for solid

cube constructs. Al-1Ni was processed first using scan speeds ranging from 400 mm/min to 1100 mm/min. Visual inspection of the build plate indicated less defects with increasing scan speed. Accordingly, the subsequent build with Al-1Fe powder shifted the range of scan speeds to 700 mm/min to 1400 mm/min (Figure 20)

Figure 20. Image of single track hollow cube specimens produced with Al-1Fe powder.

Characterization of single-track cubes was limited to a visual inspection. The relative quality for a given set of processing conditions was quantified by a linear grading scale from 0 to 3. The former corresponded to a visually defect-free part, while nonzero values correspond to the most severe of the three described defects. First, pinholes were represented by 1. Vertical cracks/voids measured as less than one half the height of the part were described as 2 while those greater than half the height of the part were assigned a grade of 3. This simple classification system allowed rapid determination of suitable processing parameters, shown in

Table 7. Al-1Ni exhibited fewer and less severe defects with increasing laser power and scan speed yet none of the process combinations considered produced a defect free product. Small pinholes were observed at 190 W and scan speeds of 800 mm/min or greater. All other processing parameter sets produced significant cracking in the final product. Al-1Fe proved to be considerably more tolerant of a wide range of processing conditions. Pinholes were observed in select samples when processed at higher scan speeds ($\geq$ 1100 mm/min). However, high scan speeds did not always produce defects, as was apparent at 170 W to

180 W and scan speeds 1200 mm/min or greater. Pinhole defects under certain parameter conditions were singular. Accordingly, the defect free specimen at these lower laser powers and faster scan speeds may have propensity for defects but were not necessarily detectable during macroscopic inspection. Between the two powder types, a 190 W laser power manifested the best possible results within the scope of this work.

Table 7. Characterization of defect severity versus process parameters for the single-track Al-1Ni and Al-1Fe specimens.

Speed (mm/s)	Al-1Ni Laser Power (W)			Al-1Fe Laser Power (W)		
	170	180	190	170	180	190
400	3	3	3	-	-	-
500	3	3	3	-	-	-
600	3	3	3	-	-	-
700	3	3	2	0	0	0
800	3	2	1	0	0	0
900	2	2	1	1	0	0
1000	2	2	1	0	0	0
1100	-	-	1	1	0	0
1200	-	-	-	0	1	1
1300	-	-	-	0	0	1
1400	-	-	-	-	-	1

3.3.2 Solid Cubes

Solid cubes were produced following satisfactory results from single track tests (Figure 21). The hatch spacing was selected to be either 120 μm or 150 μm. Laser power was fixed at 190 W to allow for a consistent range of scan speeds to be investigated with the

introduction of the hatch spacing variable. Scan speeds were again shifted towards higher rates following the trend of decreasing defect severity with increasing scan speed in Table 7. The lowest rate was chosen as 1000 mm/min given the satisfactory results for both powders at this power level. The highest rate was increased to 2000 mm/min. The process parameters for the 22 solid cubes were now fixed between the two powder types to better compare their physical properties and microstructure.

Figure 21. Solid (1cm^3) cubes produced using Al-1Fe powder.

Visual inspection of solid cubes showed that no significant surface defects were apparent under any conditions. Inferences pertaining to the quality of the surface were made using results obtained with a laser confocal microscope. Surface characteristic for the top surface as well as the side were acquired for the suite of cubes built. Surface area roughness, Sa, results were plotted against the energy input per given volume, or energy density, as shown in Figure 22. 3D surface topography images acquired from samples fabricated at the extremes of the energy density range considered (21.1 and 52.8 J/mm3) for Al-1Fe are shown in Figure 23 to compliment the surface roughness measurements. Low energy density values corresponded to higher Sa on the sides of build cubes, peaking at 38.8 μm for Al-1Ni (24.8 J/mm^3) and 38.6 μm (21.1 J/mm^3) for Al-1Fe. Surface roughness measurements for the top surfaces were generally lower for a given energy density. For instance, the top surface of Al-1Fe at 21.1 J/mm^3 measured 19.4 um, representing a

difference of 19.3 um. Similarly, in Al-1Ni built at 24.8 J/mm^3 the top surface measured 22.6 um which was 16.2 μm lower than the side value. The difference in roughness between the top and side surfaces at low energy densities manifested drastically different surface profiles. The side surface (Figure 23a) exhibited a uniform height and evenly spaced peak and valley morphology with no clear dependence with respect to the build direction. The top surface of the same cube (Figure 23b) showed a profile consistent with the raster pattern of the laser path. Along the x-axis the plot profile remained largely flat while along the y-axis it exhibited a regular wave pattern. The peak spacing appeared to match with the 150 μm hatch spacing of this specimen. Superimposed on this pattern lied occasional voids and peaks, suggesting surface porosity and unmelted particles adhered to the surface.

With greater heat input the surface characteristics improved significantly on the side surface, although the trend did not appear linear. Al-1Fe reached a minimum value of 23.9 μm at 37.7 J/mm^3 and remained between 24.3 μm and 27.3 μm for higher energy densities. Al-1Ni was comparable, reaching a minimum of 18.1 μm at 42.1 J/mm^3. The top surface again proved to have lower roughness values than the side, reaching as low as 15.7 μm for Al-1Ni and 13.5 μm for Al-1Fe, although the difference between the top and side was now significantly reduced. The side surface profile of Al-1Fe at 52.8 J/mm^3 (Figure 23c) exhibited fewer peak and valley features with larger breadth while the height of features remained of comparable magnitude. Similarly, the top surface (Figure 23d) exhibited fewer, broader features with generally less height. Interestingly, the characteristic raster path texture of the top surface was eliminated at this level of heat input. The top was generally featureless, although distinct and infrequent rounded peaks were observed. This suggested some spattering may occur at high energy densities. It is worth noting that no contours or up/downskins were applied. Their consideration in future works would likely improve surface finish but was beyond the scope of this work.
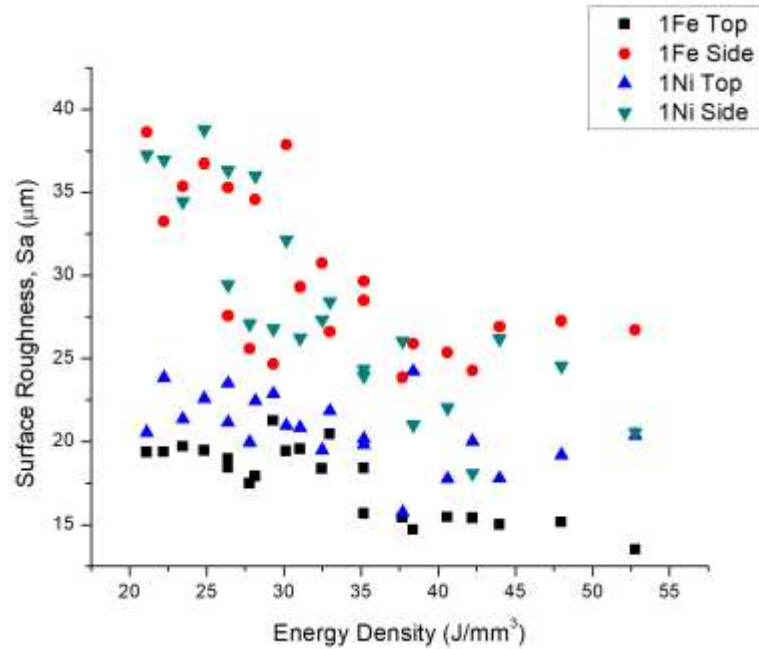
Figure 22. Effect of energy density on the roughness (Sa) of the top and side surfaces of solid cube specimens.
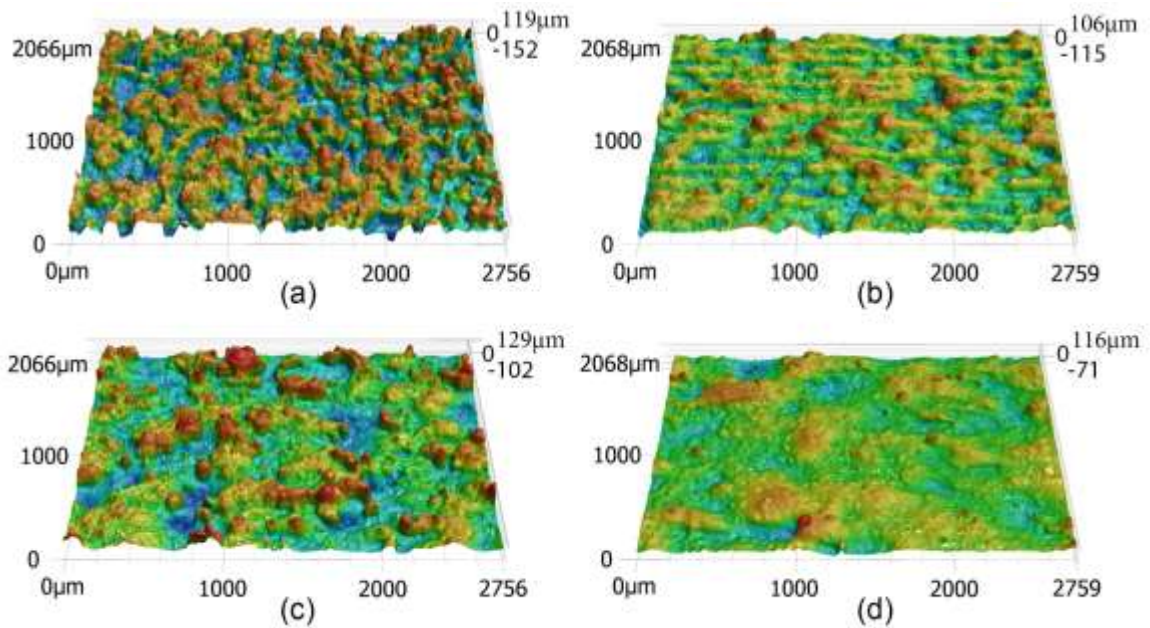

Figure 23. 3D surface height maps of Al-1Fe specimens fabricated with an energy density of 21.1J/mm^3 ((a) side, (b) top surface) and 52.8 J/mm^3 ((c) side, (d) top surface).

Data on mechanical quality was inferred through hardness measurements taken from the center of sectioned cubes. Figure 24 shows the mean values with respect to the energy density the specimens were processed at as well as indicating which hatch spacing was used. Al-1Fe reached a peak of 96 HRH when processed at 40.6 J/mm^3 (1300 mm/s, 120 µm hatch spacing), although values exceeding 91 HRH were observed as low as 27.8 J/mm^3 and persisted to the highest energy densities. Al-1Ni exhibited comparable trends in hardness albeit translated to lower values. This powder peaked to 78 HRH at 37.7 J/mm^3 (1400 mm/s and 120 um). While Al-1Fe exhibited a wider range of processing parameters that resulted in comparable hardness, Al-1Ni saw more significant decreases in hardness as processing parameters deviated from the peak hardness settings. Uniquely, the influence of hatch spacing deviated from the energy density model commonly used. For energy densities ranging from 26.4 J/mm^3 to about 42.2 J/mm^3, both Al-1Fe and Al-1Ni proved to be significantly harder when using the smaller, 120 µm hatch spacing. This suggests microstructural differences exist independent of the energy density used.
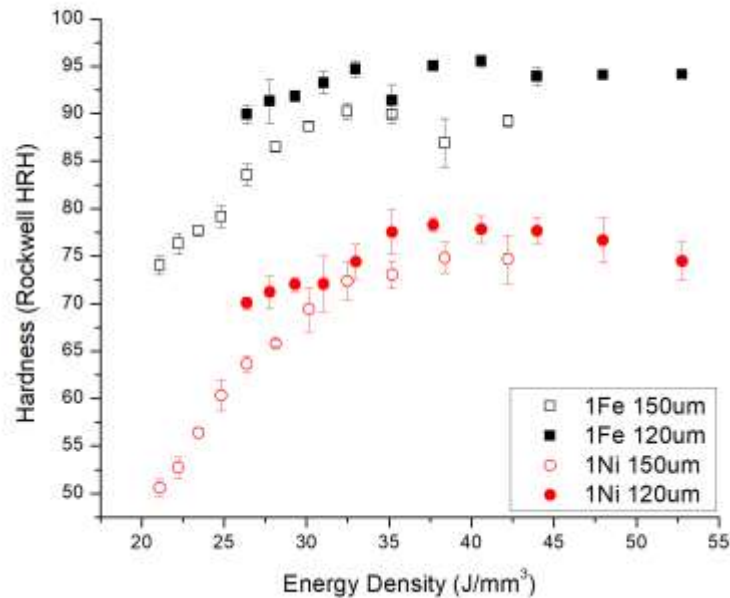

Figure 24. Effect of energy density on the hardness of as-built Al-1Fe and Al-1Ni specimens.

Densification was found to be a function of the heat input to the material. Figure 24 shows that both powders exhibited significant and rapid densification from low heat input values up to approximately 32.5 J/mm^3, followed by a domain of marginal change. Al-1Ni increased from 89.5% at 21.1 J/mm^3 to 97.2% at 32.5 J/mm^3. Density plateaued at this level, measuring between 96.6% and 97.8% at al higher energy densities. Al-1Fe faired significantly better for any given heat input, increasing from a low of 91.9% at 21.1 J/mm^3 to 98.2% at 32.5 J/mm^3. Increased energy densities resulted in marginal difference in density, ranging from 98.0% to 99.0%. For any condition, the Al-1Fe powder exceeded the Al-1Ni powder by a mean value of 1.5%.
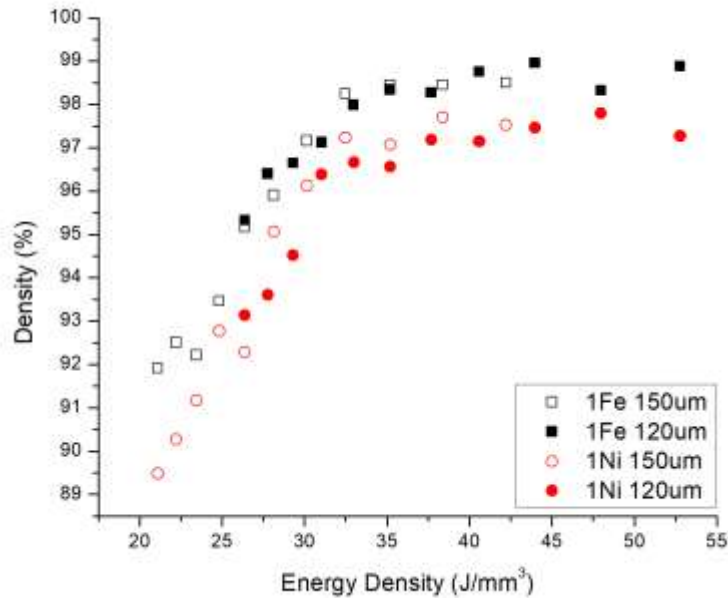
Figure 25. Effect of energy input on the relative densities of solid cube specimens.

Despite the comparable density values under various processing conditions, optical micrographs of Al-1Fe processed at 33.0 J/mm^3 to 98.0% (Figure 26a) and at 52.8 J/mm^3 to 98.9% (Figure 26b) show significant microstructural differences. The heat input at 33.0 J/mm^3 was adequate to successfully melt particles and fuse them to form a monolithic part. However, residual porosity with an irregular shape and relatively wide size distribution

persisted throughout the microstructure. At 52.8 J/mm^3 pores remained distributed throughout, although they now were now rounded and with apparently less variation in size. For comparable processing conditions the micrographs of the Al-1Ni powder revealed its inferior final density. At 33.0 J/mm^3 (Figure 27a) pores appeared in a manner comparable to Figure 26a, albeit with more irregularity. Additionally, instances of unmelted particles were observed within pores, indicating insufficient laser power for complete melting. When processed at 52.8 J/mm^3 (Figure 27b) pore irregularity was eliminated in favor of rounded uniform pores. Unmelted particles were absent. However, throughout the microstructure fine vertical cracks were observed. These appeared to pass through residual pores as well as solely through the bulk of the microstructure.

Further evidence of cracks is shown in representative optical micrographs of etched specimen (Figure 28). Al-1Fe exhibited the characteristic weld pattern of a SLM-processed specimen with vertical, epitaxial, grains translating across multiple weld tracks. Residual pores were found within individual weld tracks, near the bottom of their prior melt pool boundary. No evidence of cracking was observed throughout the bulk of the material. Al-1Ni on the other hand showed many fine and vertical cracks throughout. The etched microstructure suggests these cracks persist along vertical grain boundaries that pass over several weld tracks.

Electron micrographs near the lower boundary of the prior melt pool are shown for both powders processed at 32.5 J/mm^3 in Figure 29. Vertical grain boundaries passing through the melt pool boundary are evident and no small equiaxed grains were observed for either material. Above the melt boundary both material systems exhibited a cellular structure highlighted by regions of light contrast. Light-contrast regions found in both Al-1Fe (Figure 29c) and Al-1Ni (Figure 29d) were assessed using EDS. Such regions were found to be locally enriched in the solute but not to a level suggestive that a particular intermetallic phase was present.
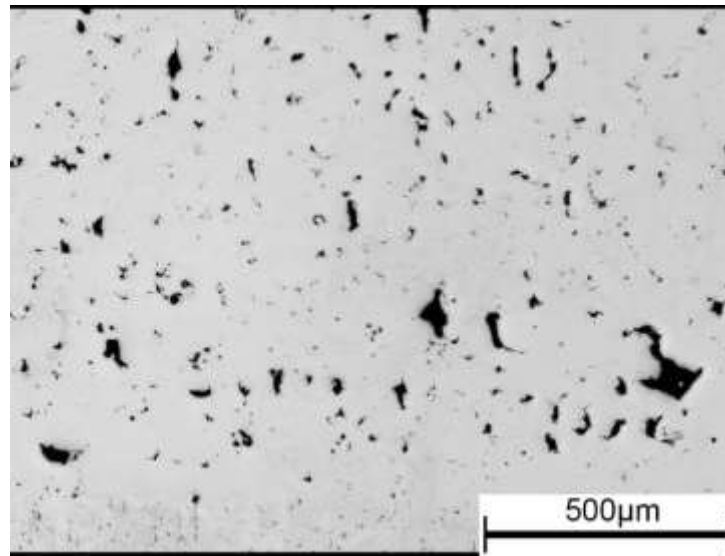
(a)
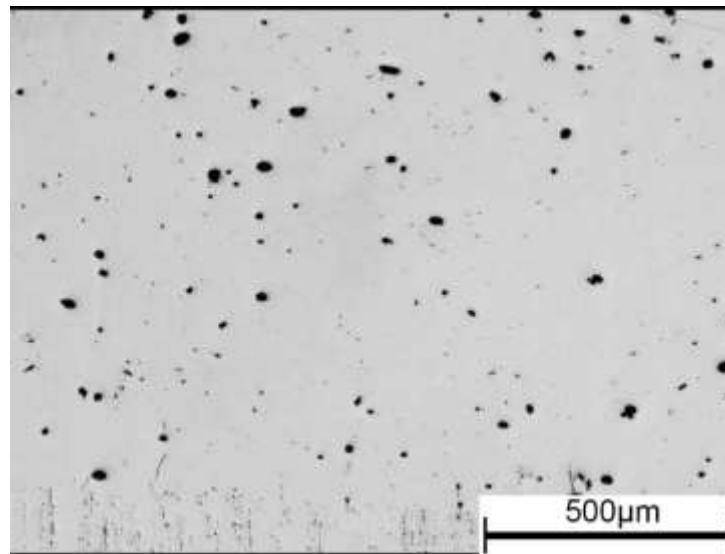
(b)

Figure 26. Optical micrographs recorded from Al-1Fe specimens processed at energy densities of (a) 33.0 J/mm^3 and (b) 52.8 J/mm^3.
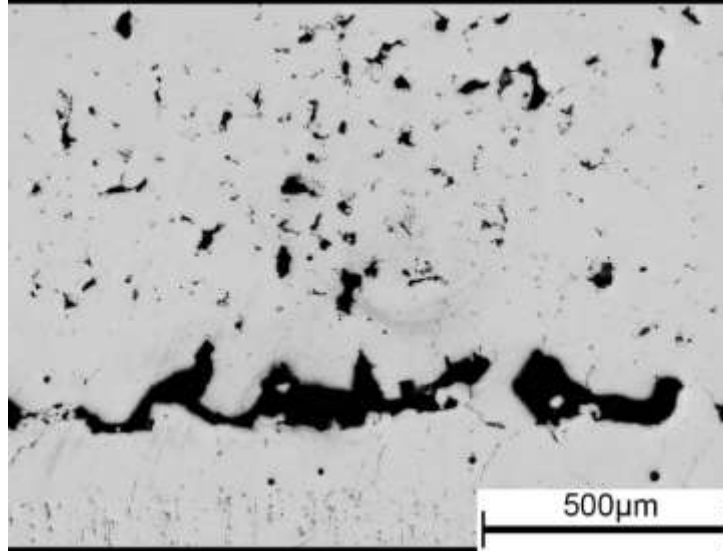
(a)
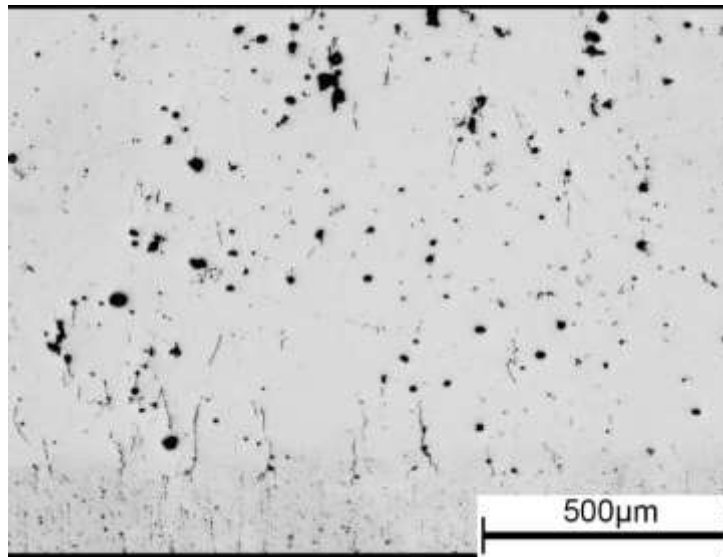
(b)

Figure 27. Optical micrographs recorded from Al-1Ni specimens processed at energy densities of (a) 33.0 J/mm^3 and (b) 52.8 J/mm^3.
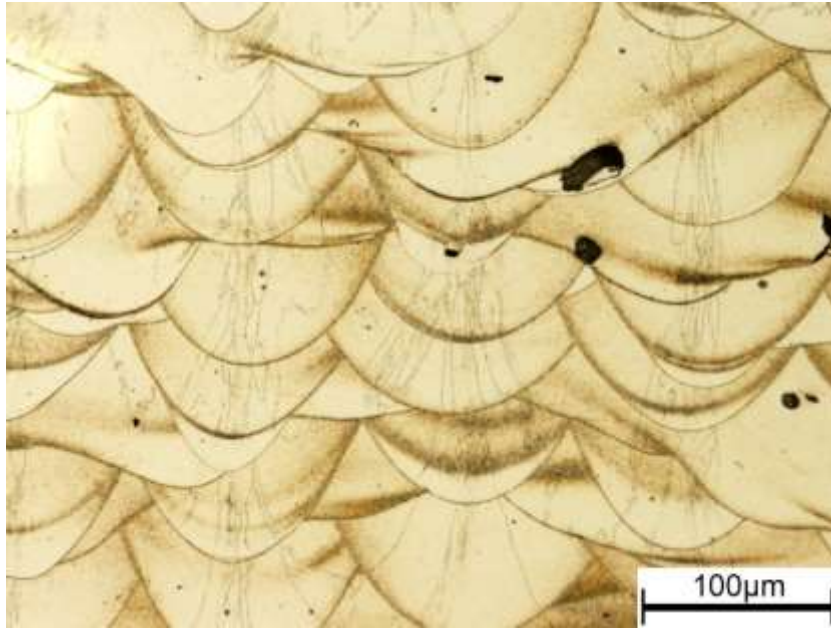
(a)
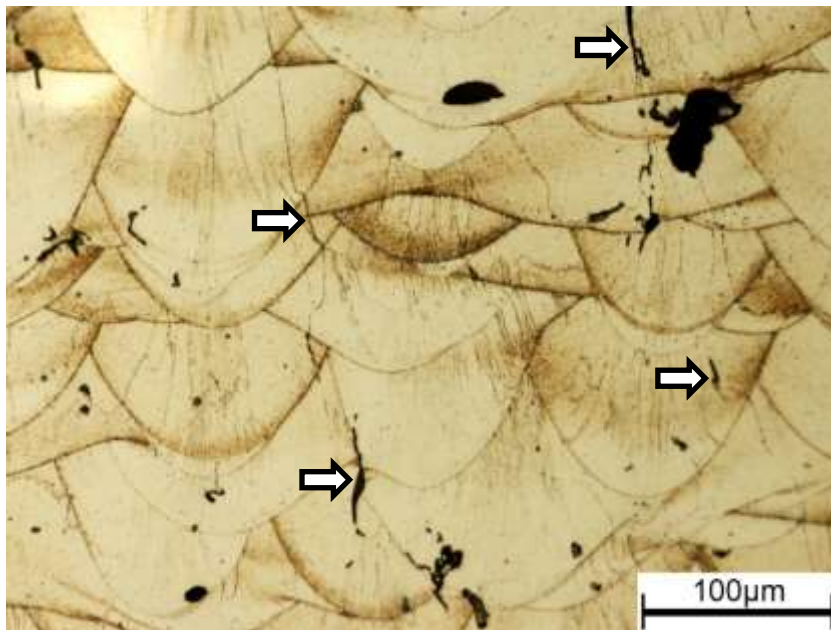
(b)

Figure 28. Optical micrographs of (a) Al-1Fe and (b) Al-1Ni processed at 52.8 J/mm^3 showing the vertical grain structure and grain boundaries, residual porosity morphology and cracks (indicated with arrows) observed along grain boundaries. Etched with Keller's reagent.
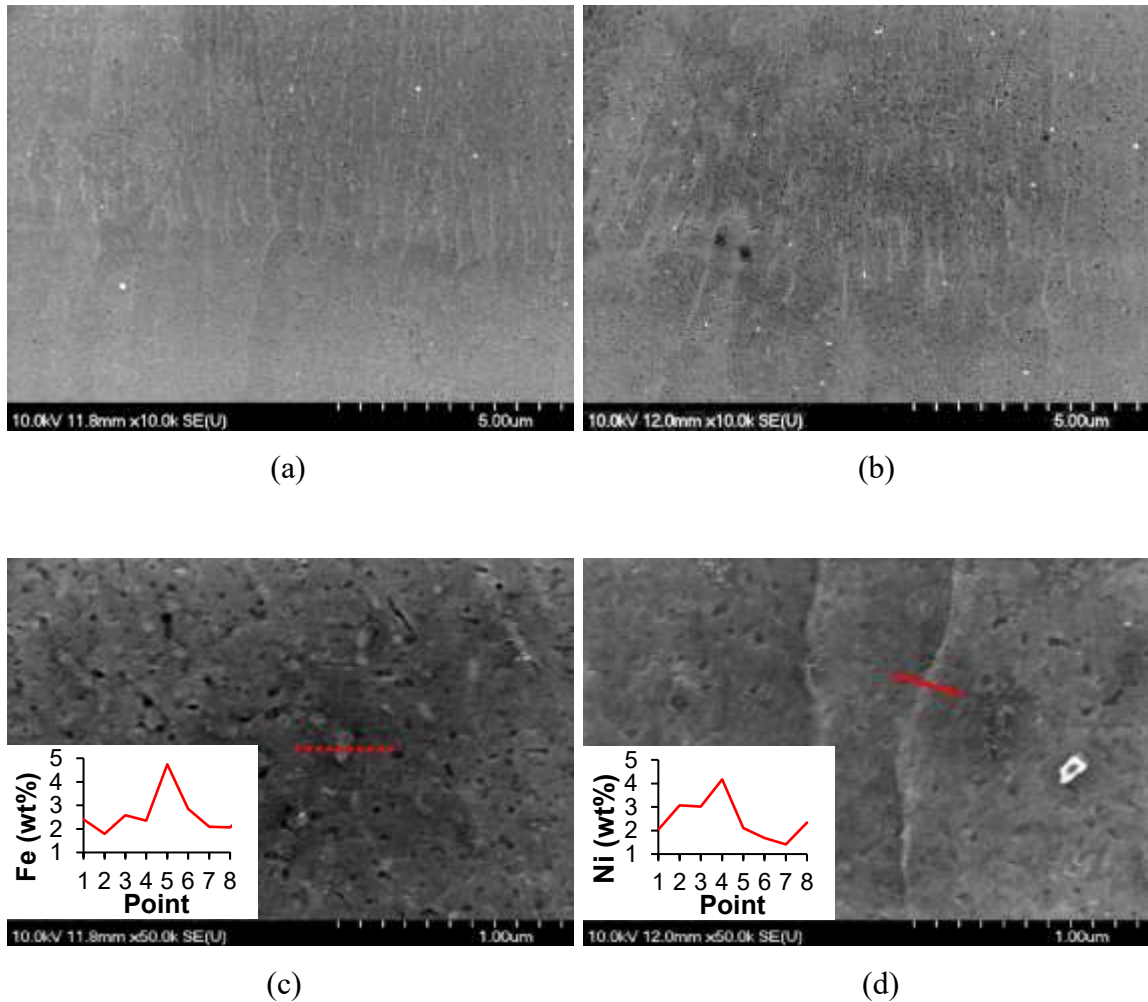
Figure 29. Electron micrographs of (a) Al-1Fe and (b) Al-1Ni processed at 32.5 J/mm³ (1300 mm/s and 150 um) showing solute rejection near the melt pool boundary. Corresponding EDS line measurements are superimposed on electron micrographs for (c) Al-1Fe and (d) Al-1Ni.

Al-1Fe and Al-1Ni specimens printed at an energy density of 21.2 J/mm³ were subsequently annealed at 530 ˚C for 4 hours. These samples were selected as they were produced with the lowest energy input. Low energy input has been correlated to high solidification front velocities (SFVs) [27]. Therefore, it was expected that the 21.1 J/mm³ samples should have the greatest deviation from equilibrium and in turn the greatest response to heat treatment. The microstructures of these samples were assessed via electron microscopy and X-ray diffraction. When using the former, solute-rich second phase

particles were readily observed in the microstructures of both annealed samples. EDS showed light contrasting particles in the Al-1Fe sample (Figure 30a) were shown to have the approximate composition of $Al_9Fe_{0.7}Ni_{1.3}$ (Al_9FeNi), while those in the Al-1Ni sample (Figure 30b) were seen to have the approximate composition of Al_9Ni_2. Relevant compositional data and micrographs can be found in Appendix A.

(a)   (b)
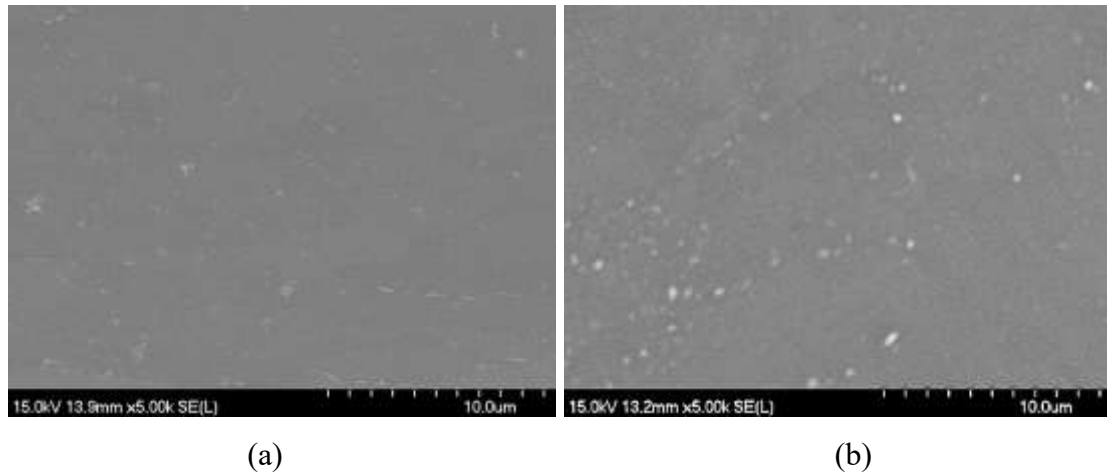
Figure 30. Electron micrographs showing fine precipitates in (a) Al-1Fe and (b) after annealing at 530 ˚C for 4 hours

X-ray diffraction traces recorded from the samples are shown in Figure 31. Plots are scaled to show 5% of the highest intensity α-Al peak to highlight minor secondary peaks. Data on both Al-1Ni and Al-1Fe specimens in the as-printed condition failed to conclusively identify the presence of known stable or metastable intermetallic phases within the 2019 version of the International Center for Diffraction Data (ICDD) database. However, once annealed, the presence of secondary phases was more apparent. For Al-1Ni, peaks associated with stable Al_3Ni were observed and select peaks matched the metastable phase Al_9Ni_2 as published by Blobaum et al [76]. However, significant overlap of these peaks with Al_3Ni and α-Al prohibited conclusive identification. Annealed Al-1Fe exhibited peaks associated with several intermetallic phases. These were primarily identified to match $Al_9Fe_{0.7}Ni_{1.3}$ (Al_9FeNi) while other peaks were associated with stable $Al_{13}Fe_4$ and metastable Al_6Fe; all phases exhibited degrees of overlap with each other.

59
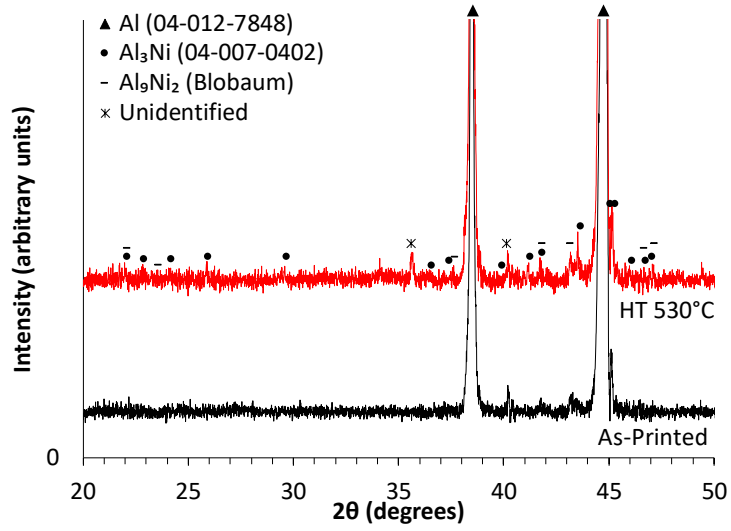
(a)
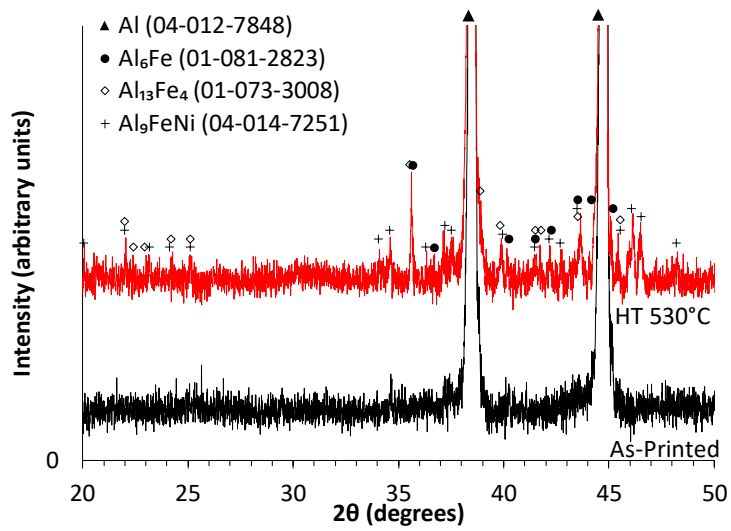
(b)

Figure 31. X-ray diffraction patterns recorded from specimen in the as-printed condition as and after annealing at 530°C for 4h. (a) Al-1Ni and (b) Al-1Fe with select intermetallic peaks identified [76]. All specimen printed at an input energy density of 21.1 J/mm^3.

3.4 Discussion

3.4.1 Solidification Cracking

The nickel-alloyed powder was shown to be less amenable to PBF-AM than its iron-bearing counterpart, as fine vertical cracks were evident throughout the microstructure of the Al-1Ni cubes. These cracks had likely contributed to both the diminished density and hardness values relative to the Al-1Fe cubes and were mainly observed at the boundaries between columnar grains (Figure 28b).

Such features can be attributed to solidification cracking. Here, cracks form near the end of solidification, when the liquid fraction in the mushy zone is reduced to a thin, intergranular liquid film [38]. As temperature decreases, solidification shrinkage can create strains sufficient to tear the film [14]. If liquid flow from the melt to the film is obstructed by a network of dendrite arms within the intergranular channels, the tear cannot be back-filled and a small cavity will be formed [3], [14], [38]. As temperature continues to decrease, residual stresses caused by thermal contraction can cause a crack to nucleate at the cavity which then propagates along the grain boundary [14].

The solidification range of an alloy commonly correlates to solidification cracking behavior, and is dependant on alloy chemistry [8]. Alloys with a large solidification range are particularly prone to solidification cracking [3], [8], [14], [21], [37], [38], as the accumulated thermal strain is proportional to the temperature range over which the alloy solidifies [8]. Conveniently, the change in solidification range per percent alloying addition in a binary alloy can be quantified using the relative potency factor (RPF), given by:

$$RPF = \frac{m_L(k-1)}{k} \qquad \qquad 3)$$

where m_L is the slope of the liquidus curve, and k is the partitioning coefficient of the binary system, which is defined as the ratio of solute in the solid phase to solute in the liquid phase [8], [77]. Additions with small k values segregate strongly to the liquid, which

makes them more prone to dendritic solidification and solidification cracking, and therefore have higher RPFs [13], [77]. Also, additions with large m_L values will have large RPF values, as they rapidly depress the liquidus temperature with increased content [8].

3.4.2 Solidification Front Velocity-Dependent Parameters

While the RPF can be of use for processes with SFVs, it is important to note that both k and m_L are dependent on SFV [29]. SFVs observed in PBF-AM are quite high, typically between 0.1 ms^{-1} and 5 ms^{-1} [26], and can invoke solute trapping [26], [28]–[30]. Solute trapping leads to extended solid solubility and k values that trend towards 1 (ie. no solute segregation) [28]–[30]. Fortunately, a velocity dependent partitioning coefficient (k^v) can be estimated using the Continuous Growth Model presented by Aziz [30]:

$$k^v = \frac{k_{eq} + \left(SFV \cdot {}^{a_o}/_{D_L}\right)}{1 + \left(SFV \cdot {}^{a_o}/_{D_L}\right)} \qquad 2)$$

Where k_{eq} is the equilibrium partitioning coefficient, D_L is the diffusivity of the alloying addition in the liquid phase, and a_o is a length scale related to the interatomic distance of atoms in the primary solidification phase. Moreover, once k^v has been solved for, a velocity dependent m_L^v can be determined using the relationship presented by Plotkowski et al [29] as shown in equation 8). k^v and m_L^v values can then be substituted into equation 3) to estimate RPF values as a function of SFV.

$$m_L^v = m_L \left(1 + \frac{k_{eq} - k^v\left[1 - \ln\left(k^v/k_{eq}\right)\right]}{1 - k_{eq}}\right) \qquad 8)$$

3.4.3   Relative Potency Factor of Al-1Fe and Al-1Ni in PBF-AM

RPF values for Al-1Fe and Al-1Ni were estimated for a range of SFVs using MATLAB and are plotted in Figure 32. Equilibrium liquidus data for the L + α-Al phase field of both alloy systems were obtained using FactSage thermodynamic modeling software (version 7.3) and fit to a polynomial. The resulting polynomials were then differentiated at 1 wt.% for each system to obtain m_L values of -3.51 and -2.61 for Al-1Fe and Al-1Ni, respectively. A list of all other constants used is shown in Table 8.
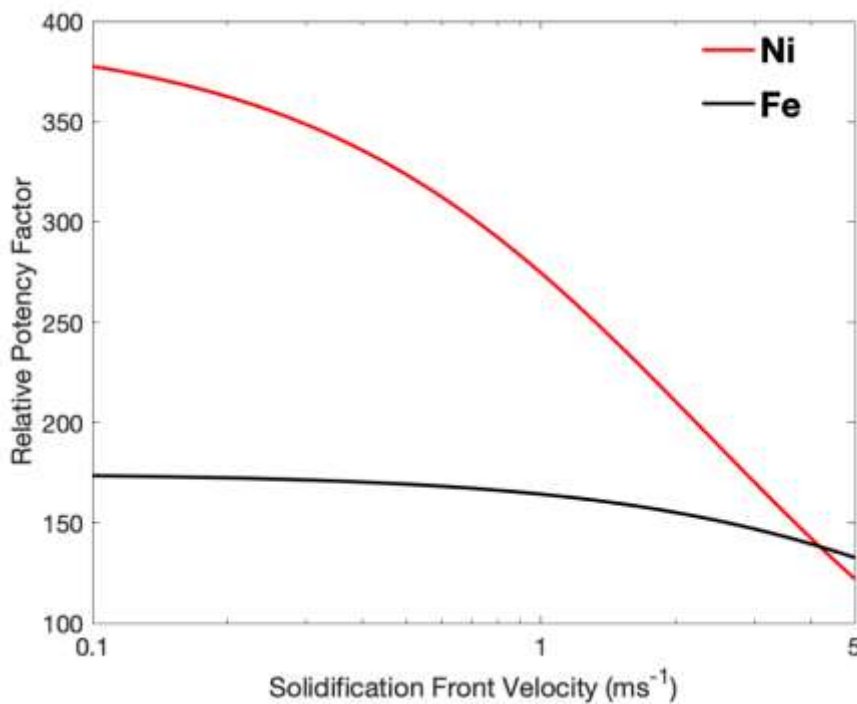
Figure 32. Relative potency factors of Al-1Fe and Al-1Ni at solidification front velocities typical of PBF-AM.

Table 8. Constants utilized in estimating the RPF for Al-1Fe and Al-1Ni systems.

Constant	Value	Units	Ref.
a_o	2.861×10^{-10}	m	Calculated
Al-1Fe			
k_{eq}	0.02	-	[77]
D_L	2.33×10^{-7}	m^2s^{-1}	[78][1]
Al-1Ni			
k_{eq}	0.007	-	[77]
D_L	9.54×10^{-8}	m^2s^{-1}	[78][1]

It is clearly seen in Figure 32 that Al-1Ni has a significantly greater propensity for solidification cracking than Al-1Fe for most of the SFVs typical of PBF-AM. A large contributing factor to this is the extremely small k^v values of Al-1Ni compared to that of Al-1Fe, as shown in Figure 33. Such small k^v values indicate that the segregation of Ni will be stronger than that of Fe at all the SFVs considered. Therefore, Al-1Ni will be more conducive to dendritic solidification and subsequent solidification cracking. At only the highest SFVs does Al-1Ni become marginally less prone to solidification cracking. This is likely because the D_L of Fe in liquid Al is greater than that of Ni. The higher D_L causes Fe to diffuse more rapidly into the liquid, which in turn hinders solute trapping at low SFVs [29]. Because of this, exceedingly high SFVs are required to cause significant increase in the k^v value of Al-1Fe. Therefore, solidification cracking in the Al-1Fe is more likely only at exceedingly high SFVs, where k^v values of the Al-1Ni system are comparable to those of Al-1Fe.

---

[1] Liquid diffusivities were estimated using the Arrhenius Equation and parameters provided by Du et al [78]. They were calculated at a temperature of 660 ˚C, the melting temperature of pure Al, and assumed to be constant.
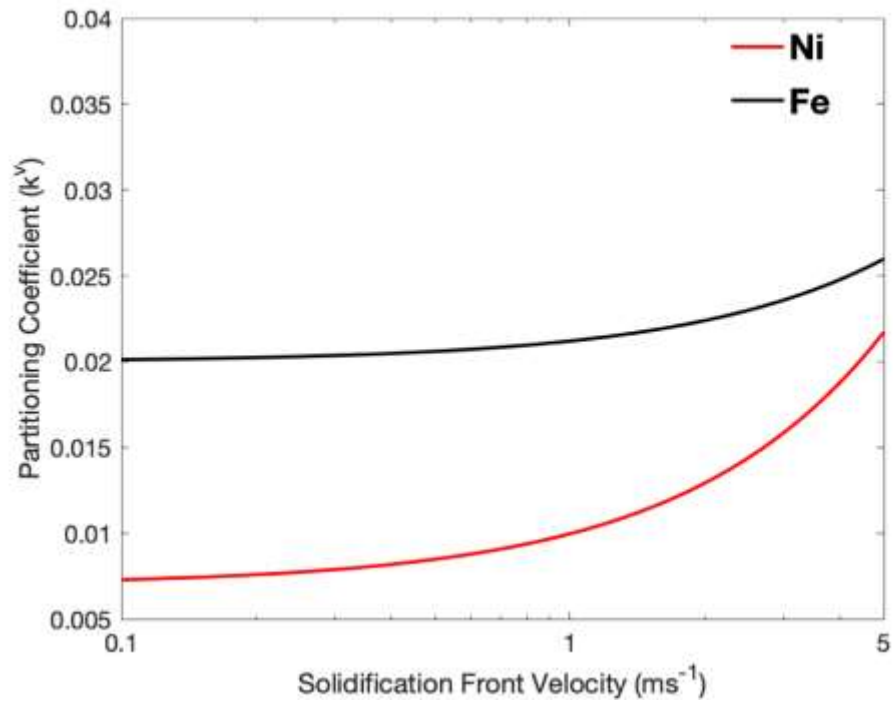
Figure 33. Calculated non-equilibrium partitioning coefficients of the Al-Fe and Al-Ni systems at solidification front velocities typical of PBF-AM.

3.4.4   Thermal Stability

Both EDS and XRD investigations of as-printed parts were unable to definitively prove the existence of stable equilibrium phases (i.e. $Al_{13}Fe_4$, Al_3Ni, etc.) in as-printed specimens. However, solute-rich regions were identified in intercellular regions near the melt pool boundaries. As the distance from the melt pool boundary increased these solute-rich areas discretized and eventually disappeared. Given that the SFV is known to increase with increasing distance from the melt boundary [10], the rate was evidently sufficient to impede the formation of thermodynamically stable phases Al_3Ni or $Al_{13}Fe_4$ in the printed specimen. Given the low solubility of both Fe and Ni in solid aluminum at any temperature, these additions would persist as stable dispersoids below the eutectic temperature.

Extremely fine (< 100nm) secondary phase particles were apparent in the microstructure (Figure 29) and suggests the as-printed samples may be nano-structured in nature. Prolonged annealing at 530°C was required evolve the microstructure into a condition more synonymous with an equilibrium-like material. Only under these conditions could plausible identities be resolved for discrete phases in each material via EDS and XRD, which corresponded to a mixture of stable and metastable phases. The persistence of metastable phases after such an excessive heat treatment is suggestive that these intermetallics would be beneficial to the thermal stability of alloys that contain additions of Fe and Ni.

3.5   Conclusions

Al-1Fe and Al-1Ni prealloyed powders were successfully processed by PBF-AM into monolithic cubes under various printing parameters. Al-1Ni exhibited improving densification as a function of energy density input, plateauing between 97.2% and 97.8% when processed at a printed energy density input of at least 32.5 J/mm^3. Residual porosity was either irregular at lower energy densities to spherical at high energy densities. The densification behavior of Al-1Fe was comparable to Al-1Ni, albeit marginally superior for any given condition. Densities of 98.2% to 99.0% were observed when processed at or above 32.5 J/mm^3. Likewise, Al-1Fe exhibited a significantly higher peak hardness of 96 HRH compared to 78 HRH for Al-1Ni. Microstructurally, all as-built specimen exhibited epitaxial grain growth and contained an abundance of nano-scale secondary phases. Prolonged high temperature annealing at 530°C was required to coarsen these phases to an observable extent suggestive that the secondary phases may be advantageous from a thermal stability standpoint. Interestingly, Al-1Ni microstructures possessed fine grain boundary cracks parallel to the build direction while Al-1Fe was produced without any detectable cracking. The increased acuity to cracking in Al-1Ni was explained by higher calculated values of relative potency factor (RPF) with respect to the solidification front velocities (SFV) typically encountered in PBF-AM.

3.6   Acknowledgements

4 SUMMARY AND CONCLUSIONS

This research successfully evaluated and compared the PBF-AM processing response of aluminum powders modified with prealloyed additions of Fe and Ni. This was accomplished by first producing thin walled single-track samples under a broad range of processing conditions to establish a nominal window of feasible parameters. Solid samples of each alloy were then produced under conditions within the established range and the as-printed properties and microstructures were characterized. Select specimens were subsequently heat treated and the resulting microstructures were characterized. From there, the Continuous Growth Model and relative potency factor were employed to establish and compare the propensity for the TM additions to cause solidification cracking during PBF-AM.

4.1 Response to PBF-AM Processing

The response of both alloys was characterized through density and hardness measurements, optical and electron microscopy, electron dispersive x-ray spectroscopy, and x-ray diffraction. Each of these measurement techniques was critical in gaining an understanding of the underlying metallurgy.

4.1.1 Physical Properties

The densification behavior of both powders was largely comparable. In this sense, relative to the starting powder bed, each powder densified appreciably as a result of PBF-AM. Additionally, the densification behaviour of both powders was seen to be a function of energy input. As energy inputs increased, the density of both powders was seen to increase significantly, until a plateau was reached at approximately 32.5 J/mm^3 above which only marginal increases were realized. Despite these similarities, the Al-1Fe powder builds were consistently denser. On average, the gain was ~1.5% of full theoretical density.

Hardnesses varied with respect to energy input in a manner comparable to that noted for density. However, as processing parameters deviated from those of the highest hardness

specimen, the Al-1Ni powder exhibited a more significant decrease. Additionally, specimens processed with a hatch spacing of 120 μm were found to consistently have higher hardness than those produced with similar energy densities and a wider hatch spacing of 150 μm. This was likely because the smaller hatch spacing afforded a higher degree of overlap between adjacent tracks which in turn allowed for more complete bonding between them. Akin to density data, the measured hardnesses of the Al-1Fe builds were also found to be higher than those of specimen produced from the Al-1Ni powder. The advantageous position of Al-1Fe prevailed under all processing conditions considered.

4.1.2 Microstructural Characterization

Optical and electron microscopy studies indicated that all as-built samples exhibited epitaxial growth with grains elongated in a direction that was nominally parallel to the build direction. No evidence of a widespread equiaxed grain structure was observed. Residual porosity was visually apparent in both materials. It was generally irregular in shape at low energy densities but transitioned toward a more spherical shape as energy input increased. This transition was more pronounced in the Al-1Fe specimens.

Microscopy also revealed cellular structures near melt pool boundaries in both alloys. Electron dispersive x-ray spectroscopy (EDS) implied that the intercellular regions were enriched with the respective alloying addition, but not to concentrations that would suggest the presence of a second phase. Additionally, no known equilibrium or metastable phases could be definitively identified by x-ray diffraction (XRD) in any of the as-built specimens regardless of powder chemistry.

After heat treatment at 530 ˚C for 4 hours, nano-scaled secondary phases were apparent in both materials. XRD was then used for phase identification. In all cases, the resultant traces were complex and contained a significant number of minor secondary peaks. This was suggestive of a complex microstructure and complicated definitive phase analysis. Data from the Al-1Fe specimen indicated the likely presence of Al_9FeNi, $Al_{13}Fe_4$ and metastable

69

Al$_6$Fe. Analysis of Al-1Ni specimen implied that Al$_3$Ni was present, although some peaks were a reasonable match for the metastable phase Al$_9$Ni$_2$ as well. The continued presence of nano-sized, and possibly metastable, phases in both materials after this aggressive heat treatment was suggestive that Fe and Ni may offer enhanced thermal stability to Al alloys processed by PBF-AM.

4.2   Amenability to PBF-AM

Fine cracks in the boundaries between epitaxial grains were seen to persist through multiple build layers in many of the Al-1Ni specimens. However, no such cracks were observed in Al-1Fe counterparts. These cracks were identified as solidification cracks and were potentially a contributing factor to the comparatively lower density and hardness measured in the Al-1Ni builds. Therefore, the propensity for solidification cracking was used to assess and compare the amenability of Al-1Fe and Al-1Ni to PBF-AM, as determined by calculated k^v values and SFV-dependent relative potency factors.

k^v values were first estimated using the Continuous Growth Model. An extremely small k_{eq} value was noted for the Al-Ni system. It was postulated that this had likely increased the propensity to form solidification structures that would have inhibited liquid feeding. Furthermore, the effects of increased SFV on k^v were expected to be more pronounced on Al-1Ni as a result of the lower liquid diffusivity of Ni in Al when compared that of Fe. SFV-dependent RPF values were subsequently calculated, and showed Al-1Fe to be less prone to solidification cracking at almost all SFVs typically encountered in PBF-AM. Only at the highest SFVs was Al-1Ni expected to become comparably prone to solidification cracking. Collectively, these calculations were supportive of the increased propensity for solidification cracking in Al-1Ni builds.

4.3   Future Works

There are several other studies that could not be explored due to time constraints. Recommendations for future research include:

1. Obtaining a more complete understanding of mechanical properties and their dependencies on processing parameters. This could be done by performing tensile testing on specimens of both chemistries produced under varying conditions.

2. Obtaining a better understanding of the precipitation behaviour observed in the annealed specimens. This could be done using differential scanning calorimetry (DSC) and/or dilatometry which would also allow for the thermal stability of both systems to be compared.

3. A similar characterization of the Al-Fe-Ni system. The ternary system is known to form thermally stable intermetallic phases, but processability currently unknown.

4. An investigation into of Zr additions a cost-effective means to improve processability and properties through the formation of grain refining Al_3Zr.

REFERENCES

[1] D. Gu, *Laser Additive Manufacturing of High-Performance Materials*, First. Berlin, Heidelberg: Springer Berlin Heidelberg, 2015.

[2] ASTM International, "F3318-18 Standard for Additive Manufacturing – Finished Part Properties – Specification for AlSi10Mg with Powder Bed Fusion – Laser Beam," 2018.

[3] S. Lathabai, *Additive Manufacturing of Aluminium-Based Alloys and Composites*. 2018.

[4] Y. Ding, J. A. Muñiz-Lerma, M. Trask, S. Chou, A. Walker, and M. Brochu, "Microstructure and mechanical property considerations in additive manufacturing of aluminum alloys," *MRS Bull.*, vol. 41, no. 10, pp. 745–751, 2016.

[5] K. E. Knipling, "Development of a Nanoscale Precipitation-Strengthened Creep-Resistant Aluminum Alloy Containing Trialuminide Precipitates," 2006.

[6] J. R. Croteau *et al.*, "Microstructure and mechanical properties of Al-Mg-Zr alloys processed by selective laser melting," *Acta Mater.*, vol. 153, pp. 35–44, 2018.

[7] K. E. Knipling, D. C. Dunand, and D. N. Seidman, "Criteria for developing castable, creep-resistant aluminum-based alloys - A review," *Zeitschrift für Met.*, vol. 97, no. 3, pp. 246–265, 2006.

[8] ASM International, *Volume 6: Welding, Brazing and Soldering*. ASM International, 1993.

[9] S. Marola *et al.*, "A comparison of Selective Laser Melting with bulk rapid solidification of AlSi10Mg alloy," *J. Alloys Compd.*, vol. 742, pp. 271–279, 2018.

[10] S. Griffiths, M. D. Rossell, J. Croteau, N. Q. Vo, D. C. Dunand, and C. Leinenbach, "Effect of laser rescanning on the grain microstructure of a selective laser melted Al-Mg-Zr alloy," *Mater. Charact.*, vol. 143, no. March, pp. 34–42, 2018.

[11] P. . Smith and M. J. Aziz, "Solute Trapping in Aluminum Alloys," *Acta Metall. Mater.*, vol. 42, no. 10, pp. 3515–3525, 1994.

[12] M. A. Otooni, *Elements of Rapid Solidification*, vol. 29. 1998.

[13] M. Flemings, *Materials Science and Engineering Series - Solidification & Casting*. 1974.

[14] M. Rappaz, J. M. Drezet, and M. Gremaud, "A new hot-tearing criterion," *Metall. Mater. Trans. A*, vol. 30, no. 2, pp. 449–455, Feb. 1999.

[15] I. Gibson, D. W. D. W. Rosen, and B. Stucker, *Additive Manufacturing Technologies: Rapid Prototyping to Direct Digital Manufacturing*, vol. 54. 2009.

[16] ASTM International, "F2792-12a - Standard Terminology for Additive Manufacturing Technologies," *Rapid Manuf. Assoc.*, pp. 10–12, 2013.

[17] A. J. Pinkerton, "[INVITED] Lasers in additive manufacturing," *Opt. Laser Technol.*, vol. 78, pp. 25–32, 2016.

[18] H. Lee, C. H. J. Lim, M. J. Low, N. Tham, V. M. Murukeshan, and Y. J. Kim, "Lasers in additive manufacturing: A review," *International Journal of Precision Engineering and Manufacturing - Green Technology*, vol. 4, no. 3. pp. 307–322, 2017.

[19] A. T. Sutton, C. S. Kriewall, M. C. Leu, and J. W. Newkirk, "Powder characterisation techniques and effects of powder characteristics on part properties in powder-bed fusion processes," vol. 12, no. 1, pp. 3–29, 2017.

[20] S. Sun, M. Brandt, and M. Easton, "Powder bed fusion processes: An overview," in *Laser Additive Manufacturing: Materials, Design, Technologies, and Applications*, Elsevier Ltd, 2016, pp. 55–77.

[21] A. I. Mertens, J. Delahaye, and J. Lecomte-Beckers, "Fusion-Based Additive Manufacturing for Processing Aluminum Alloys: State-of-the-Art and Challenges," *Adv. Eng. Mater.*, vol. 19, no. 8, 2017.

[22] K. Thyagarajan and A. Ghatak, *Lasers: Fundamentals and Applications*, vol. 53, no. 9. 2010.

[23] J. G. Eden, "Laser technology: theory and operating principles," *IEEE Potentials*, vol. 4, no. 2, pp. 7–12, 1985.

[24] W. Kurz and D. J. Fisher, "Fundamentals of solidification." 1992.

[25] S. Kou, *Welding Metallurgy*. Hoboken, NJ, USA: John Wiley & Sons, Inc., 2002.

[26] J. H. Martin, B. D. Yahata, J. M. Hundley, J. A. Mayer, T. A. Schaedler, and T. M. Pollock, "3D printing of high-strength aluminium alloys," *Nature*, vol. 549, no. 7672, pp. 365–369, 2017.

[27] D. W. Heard, R. Gauvin, and M. Brochu, "Non-equilibrium solute partitioning in a laser re-melted Al-Li-Cu alloy," *Acta Mater.*, vol. 61, no. 19, pp. 7432–7436, 2013.

[28] W. Kurz, B. Giovanola, and R. Trivedi, "Theory of microstructural development during rapid solidification," *Acta Metall.*, vol. 34, no. 5, pp. 823–830, 1986.

[29] A. Plotkowski *et al.*, "Evaluation of an Al-Ce alloy for laser additive manufacturing," *Acta Mater.*, vol. 126, pp. 507–519, 2017.

[30] M. J. Aziz, "Model for solute redistribution during rapid solidification," *J. Appl. Phys.*, vol. 53, no. 2, pp. 1158–1168, 1982.

[31] M. . Aziz and T. Kaplan, "Continuous Growth Model for Interface Motion During Alloys Solidification," *Acta Metall.*, vol. 36, no. 8, pp. 2335–2347, 1988.

[32] D. W. Heard, J. Boselli, R. Rioja, E. A. Marquis, R. Gauvin, and M. Brochu, "Interfacial morphology development and solute trapping behavior during rapid solidification of an Al-Li-Cu alloy," *Acta Mater.*, vol. 61, no. 5, pp. 1571–1580, 2013.

[33] W. F. Smith, *Structure and Properties of Engineering Alloys*, 1st ed. New York: McGraw-Hill, 1993.

[34] D. Herzog, V. Seyda, E. Wycisk, and C. Emmelmann, "Additive manufacturing of metals," *Acta Mater.*, vol. 117, pp. 371–392, 2016.

[35] E. O. Olakanmi, R. F. Cochrane, and K. W. Dalgarno, "A review on selective laser sintering/melting (SLS/SLM) of aluminium alloy powders: Processing, microstructure, and properties," *Prog. Mater. Sci.*, vol. 74, pp. 401–477, 2015.

[36] D. Zhang *et al.*, "Metal Alloys for Fusion-Based Additive Manufacturing," *Adv. Eng. Mater.*, vol. 20, no. 5, pp. 1–20, 2018.

[37] J. Zhang, B. Song, Q. Wei, D. Bourell, and Y. Shi, "A review of selective laser melting of aluminum alloys : Processing, microstructure, property and developing trends," *J. Mater. Sci. Technol.*, vol. 35, pp. 270–284, 2019.

[38] N. Coniglio and C. E. Cross, "Initiation and growth mechanisms for weld solidification cracking," *Int. Mater. Rev.*, vol. 58, no. 7, pp. 375–397, 2013.

[39] K. Ellmer, *Laser-Assisted Fabrication of Materials*, vol. 161. Berlin, Heidelberg: Springer Berlin Heidelberg, 2013.

[40] W. M. Steen and J. Mazumder, *Laser Material Processing*. London: Springer London, 2010.

[41] ASM International, *Volume 2: Properties and Selection - Nonferrous Alloys and Special-Purpose Materials*. ASM International, 1992.

[42] K. E. Knipling, D. C. Dunand, and D. N. Seidman, "Criteria for developing castable, creep-resistant aluminum-based alloys - A review," *Zeitschrift für Met.*, vol. 97, no. 3, pp. 246–265, 2006.

[43] ASM International, *Volume 19: Fatigue and Fracture*. ASM International, 1996.

[44] O. Wouters, "Chapter 3: Dislocations and Precipitation Hardening," in *Plasticity in Aluminum Alloys at Various Length Scales*, 2006, p. 24.

[45] V. V. Zakharov, "About Alloying of Aluminum Alloys with Transition Metals," *Met. Sci. Heat Treat.*, vol. 59, no. 1–2, pp. 67–71, 2017.

[46] ASM International, *Volume 7: Powder Metal Technologies and Applications*, vol. 7. ASM International, 1998.

[47] T. Werz, M. Baumann, U. Wolfram, and C. E. Krill, "Particle tracking during Ostwald ripening using time-resolved laboratory X-ray microtomography," *Mater. Charact.*, vol. 90, pp. 185–195, 2014.

[48] E. J. Lavernia, J. D. Ayers, and T. S. Srivatsan, "Rapid solidification processing with specific application to aluminium alloys," *Int. Mater. Rev.*, vol. 37, no. 1, pp. 1–44, 1992.

[49] V. I. Elagin, "Ways of developing high-strength and high-temperature structural aluminum alloys in the 21st century," *Met. Sci. Heat Treat.*, vol. 49, no. 9–10, pp. 427–434, 2007.

[50] M. E. Fine, "Precipitation hardening of aluminum alloys," *Metall. Trans. A*, vol. 6, no. 4, pp. 625–630, Apr. 1975.

[51] V. Raghavan, "Al−Fe−V (Aluminum-Iron-Vanadium)," *J. Phase Equilibria Diffus.*, vol. 27, no. 3, pp. 283–283, 2006.

[52] M. L. Öveçoglu, C. Suryanarayana, and W. D. Nix, "Identification of precipitate phases in a mechanically alloyed rapidly solidified Al-Fe-Ce alloy," *Metall. Mater. Trans. A Phys. Metall. Mater. Sci.*, vol. 27, no. 4, pp. 1033–1041, 1996.

[53] Y.-W. Kim, "Advanced Aluminum Alloys for High Temperature Structural Applications," *Industrial Heating*, pp. 31–34, 1988.

[54] ASM International, *Volume 3: Alloy Phase Diagrams*, vol. 3. ASM International, 1992.

[55] S. D. Kirchoff, R. H. Young, W. M. Griffith, and Y.-W. Kim, "Microstructure/Strength/Fatigue Crack Growth Relations in High Temperature P/M Aluminum Alloys," *High-strength powder Metall. Alum. Alloy.*, pp. 237–248, 1982.

[56]   L. C. Zhang, A. Q. He, H. Q. Ye, C. Huang, and Y. C. Zhang, "Characterization of dispersed intermetallic phases in an Al-8.32wt%Fe-3.4wt%Ce alloy," *J. Mater. Sci.*, vol. 37, no. 24, pp. 5183–5189, 2002.

[57]   W. M. Griffith, R. E. Sanders, and G. J. Hidelman, "Elevated Temperature Aluminum Alloys for Aerospace Applications," in *High-strength powder metallurgy aluminum alloys*, 1982, pp. 209–224.

[58]   C. H. Shek, G. He, Z. Bian, G. L. Chen, and J. K. L. Lai, "Effect of composition and cooling rate on structures and properties of quenched or cast Al-V-Fe alloys," *Mater. Sci. Eng. A*, vol. 357, no. 1–2, pp. 20–26, 2003.

[59]   S. Yaneva, K. Petrov, R. Petrov, N. Stoichev, G. Avdeev, and R. Kuziak, "Influence of silicon content on phase development in Al-Fe-V-Si alloys," *Mater. Sci. Eng. A*, vol. 515, no. 1–2, pp. 59–65, 2009.

[60]   J. E. Spinelli, M. V Canté, N. Cheung, N. Mangelinck-Noël, and A. Garcia, "SEM Characterization of Al3Ni Intermetallics and its Influence on Mechanical Properties of Directionally Solidified Hypoeutectic Al-Ni Alloys," *Mater. Sci. Forum*, vol. 636–637, pp. 465–470, 2010.

[61]   K. Huang, "Precipitation Strengthening in Al-Ni-Mn Alloys," *Metall. Mater. Trans. A*, vol. 46, no. 12, pp. 5830–5841, 2015.

[62]   F. Hernández-Méndez, A. Altamirano-Torres, J. G. Miranda-Hernández, E. Térres-Rojas, and E. Rocha-Rangel, "Effect of Nickel Addition on Microstructure and Mechanical Properties of Aluminum-Based Alloys," *Mater. Sci. Forum*, vol. 691, pp. 10–14, 2011.

[63]   F. Trevisan *et al.*, "On the selective laser melting (SLM) of the AlSi10Mg alloy: Process, microstructure, and mechanical properties," *Materials (Basel).*, vol. 10, no. 76, 2017.

[64]   L. P. Lam, D. Q. Zhang, Z. H. Liu, and C. K. Chua, "Phase analysis and microstructure characterisation of AlSi10Mg parts produced by Selective Laser Melting," *Virtual Phys. Prototyp.*, vol. 10, no. 4, pp. 207–215, 2015.

[65]   ASM International, *Volume 9: Metallography and Microstructures*, vol. 9. ASM International, 2004.

[66]   NanoAl LLC, "Addalloy - Aluminum Alloy for AM." .

[67]   N. Q. Vo, J. R. Croteau, D. Bayansan, A. Sanaty-Zadeh, and E. Ramos, "Ribbons and powders from high strength corrosion resistant aluminum powders," WO 2018/009359 Al, 2017.

[68]   J. Forde and W. Stott, "Aluminum-Copper Alloy for Casting," US9033025B2, 2010.

[69]   Aeromet International Limited, "A20X Powder: A New, High Strength Option for Aluminum Additive Manufacturing." [Online]. Available: http://a20x.com/powder/. [Accessed: 06-Oct-2018].

[70]   T. DebRoy *et al.*, "Additive manufacturing of metallic components – Process, structure and properties," *Prog. Mater. Sci.*, vol. 92, pp. 112–224, Mar. 2018.

[71]   N. T. Aboulkhair, N. M. Everitt, I. Ashcroft, and C. Tuck, "Reducing porosity in AlSi10Mg parts processed by selective laser melting," *Addit. Manuf.*, vol. 1, pp. 77–86, Oct. 2014.

[72]   W. J. Sames, F. A. List, S. Pannala, R. R. Dehoff, and S. S. Babu, "The metallurgy and processing science of metal additive manufacturing," *Int. Mater. Rev.*, vol. 61, no. 5, pp. 315–360, 2016.

[73]   A. Aversa *et al.*, "New aluminum alloys specifically designed for laser powder bed fusion: A review," *Materials (Basel).*, vol. 12, no. 7, 2019.

[74]   K. E. Knipling, D. C. Dunand, and D. N. Seidman, "Criteria for developing castable, creep-resistant aluminum-based alloys-A review," 2006.

[75]   K. Schmidtke, F. Palm, A. Hawkins, and C. Emmelmann, "Process and mechanical properties: Applicability of a scandium modified Al-alloy for laser additive manufacturing," *Phys. Procedia*, vol. 12, no. PART 1, pp. 369–374, 2011.

[76]   K. J. Blobaum, D. Van Heerden, A. J. Gavens, and T. P. Weihs, "Al/Ni formation reactions: Characterization of the metastable Al9Ni2 phase and analysis of its formation," *Acta Mater.*, 2003.

[77]   G. K. Sigworth, "Fundamentals of Solidification in Aluminum Castings," *Int. J. Met.*, vol. 8, no. 1, pp. 7–20, 2014.

[78]   Y. Du *et al.*, "Diffusion coefficients of some solutes in fcc and liquid Al: critical evaluation and correlation," *Mater. Sci. Eng. A*, vol. 363, no. 1–2, pp. 140–151, 2003.

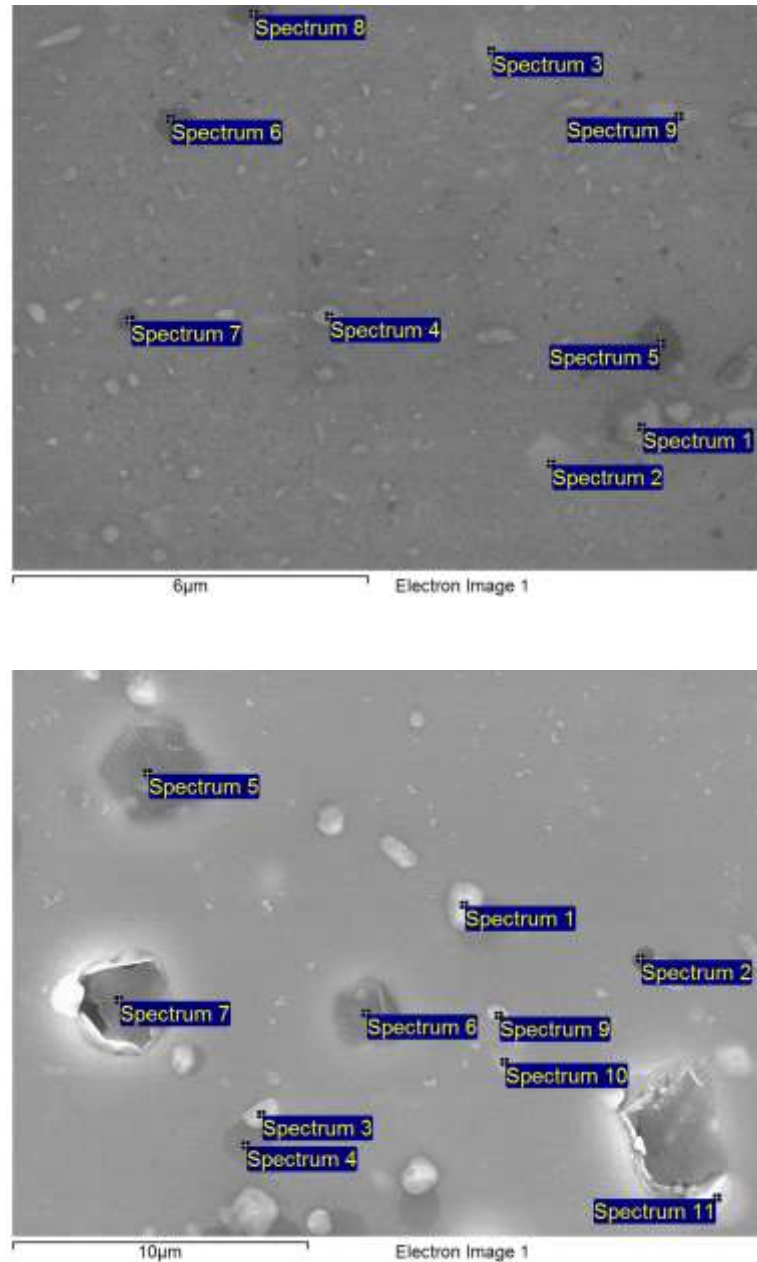# APPENDIX A – PERTINANT COMPOSITIONAL DATA OF HEAT TREATED SPECIMENS

Figure 34. Electron micrographs of heat treated Al-1Fe (top) and Al-1Ni (bottom) specimens processed at 21.1 J/mm3 showing the locations of EDS point measurements.

Table 9. Composition (wt.%) of points measured by EDS (15 kV) for the heat treated Al-1Fe and Al-1Ni specimens processed at 21.1 J/mm3.

Spectrum	Al	Fe	Ni	O
Al-1Fe				
1	92.22	3.22	3.12	1.44
2	91.87	3.90	3.10	1.12
3	92.20	3.44	3.50	0.86
4	88.58	4.91	4.83	1.68
5	96.69	0.76	1.13	1.42
6	94.96	1.79	1.86	1.40
7	95.63	1.64	1.59	1.14
8	97.16	0.81	0.76	1.27
9	89.52	3.66	5.19	1.63
Al-1Ni				
1	74.80	0.00	22.81	2.39
2	96.80	0.00	0.08	3.12
3	72.80	0.06	25.17	1.96
4	97.52	0.00	0.92	1.56
5	97.68	0.01	1.72	0.59
6	96.76	0.17	1.00	2.07
7	93.52	0.61	3.84	2.03
9	96.26	0.00	2.51	1.23
10	87.83	1.39	9.75	1.03
11	58.82	0.03	39.19	1.96